

Review

Surface-Controlled Photocatalysis and Chemical Sensing of TiO_2 , $\alpha\text{-Fe}_2\text{O}_3$, and Cu_2O Nanocrystals

Anna Kusior ^{1,*} , Milena Synowiec ¹, Katarzyna Zakrzewska ² and Marta Radecka ¹

¹ Faculty of Materials Science and Ceramics, AGH University of Science and Technology, al. A. Mickiewicza 30, 30-059 Krakow, Poland; milsyn@agh.edu.pl (M.S.); radecka@agh.edu.pl (M.R.)

² Faculty of Computer Science, Electronics and Telecommunications, AGH University of Science and Technology, al. A. Mickiewicza 30, 30-059 Krakow, Poland; zak@agh.edu.pl

* Correspondence: akusior@agh.edu.pl; Tel.: +48-12-617-2468

Received: 2 March 2019; Accepted: 7 March 2019; Published: 20 March 2019



Abstract: A relatively new approach to the design of photocatalytic and gas sensing materials is to use the shape-controlled nanocrystals with well-defined facets exposed to light or gas molecules. An abrupt increase in a number of papers on the synthesis and characterization of metal oxide semiconductors such as a TiO_2 , $\alpha\text{-Fe}_2\text{O}_3$, Cu_2O of low-dimensionality, applied to surface-controlled photocatalysis and gas sensing, has been recently observed. The aim of this paper is to review the work performed in this field of research. Here, the focus is on the mechanism and processes that affect the growth of nanocrystals, their morphological, electrical, and optical properties and finally their photocatalytic as well as gas sensing performance.

Keywords: nanocrystals; surface-controlled processes; TiO_2 ; $\alpha\text{-Fe}_2\text{O}_3$; Cu_2O ; photocatalysis; gas sensors

1. Introduction

Inorganic single crystals of metal oxides with highly reactive surfaces play a particularly important role in photocatalysis [1–6], photoelectrochemistry including hydrogen generation by water splitting [7] and, quite recently, gas sensors [8–14]. A brilliant idea to expose highly reactive facets of well-defined crystals to external stimuli such as light, gas, or organic pollutants in order to enhance the efficiency of processes governed by the surface chemistry has been exploited for a long time [15–23]. However, its practical realization has been greatly accelerated with the advent of nanotechnology [7,24]. Since 2008, when Yang et al. [25] published the results on micrometer sized, well-defined TiO_2 single crystals with a high percentage of reactive facets, one can observe a dramatically increased number of papers devoted to facet engineering of surface and interface design, especially in the application to photocatalytic materials [26–28].

Single crystals are usually terminated with the low Miller index facets that allow minimizing their surface energy. During the crystal growth, the rate, at which the high Miller index facets evolve, is very fast, eliminating them in the final state. Wulff theorem [29] predicts the most thermodynamically favored shapes of large enough single crystal nanoparticles. It states that a given crystallographic facet appears at a distance d_i from the center of particle which is proportional to its surface energy γ_i ($d_i/\gamma_i = \text{const}$). Therefore, the shape is determined by the facets that remain at a low distance from the center of a nanoparticle, being at the same time—the low energy ones.

Thus, the high energy facets, being unstable, are rarely exposed. However, a surface atomic structure plays an important role in many processes governed by adsorption and particularly chemisorption as shown in Figure 1. In many applications, such as photocatalysis and gas sensing, less chemically stable and more active facets are the most sought for because, due to a different arrangement

of atoms leading to a high concentration of dangling bonds, they facilitate, e.g., the separation of photoinduced charges in photocatalysis and adsorption of gas molecules necessary for gas sensing.

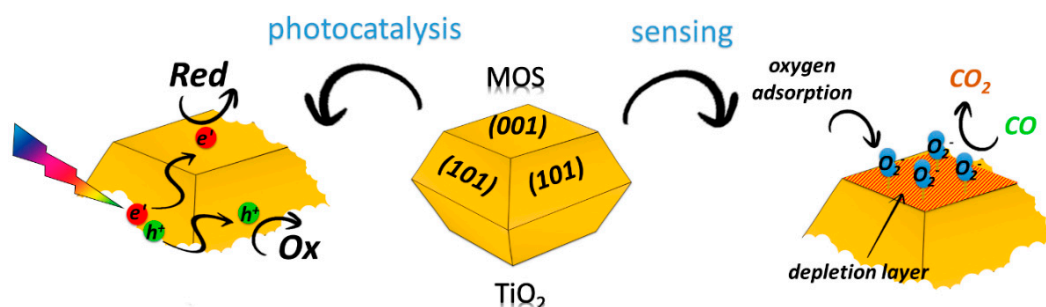


Figure 1. Mechanism of facet-dependent photocatalysis and (bio)chemical sensing for specifically shaped metal oxide semiconductor (MOS), Red—reduction, Ox—oxidation processes.

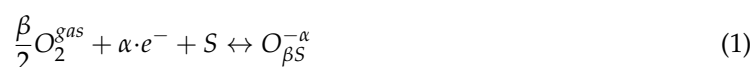
Figure 1 illustrates the idea of the facet-dependent photocatalysis and (bio)chemical sensing of metal oxide semiconductor (MOS) using as an example anatase TiO_2 crystals that are normally dominated by the thermodynamically stable $\{101\}$ facets (more than 94% according to the Wulff construction [30]) rather than much more reactive $\{001\}$ facets. However, an exposure of the more reactive $\{001\}$ facets has a tremendous impact on both photocatalysis and gas sensing mechanism.

Photocatalysis requires a control over three basic steps, as shown in Figure 1—left, concerning the charge, electrons e^- , and holes h^+ :

1. generation upon photoexcitation,
2. transfer to the surface of the photocatalytic crystal,
3. participation in redox reactions taking place at the active surface.

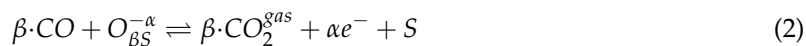
Charge kinetics in all these processes decides about the overall efficiency of the photocatalysis while in the case of shape-controlled crystals, the transfer of electrons and holes to different facets may help in avoiding too fast recombination, being detrimental to the efficiency of the process. However, as explained later, in Section 4, the exposed facets may affect the photocatalytic performance through multiple effects.

Gas sensing by metal oxide semiconductors, MOS, is usually based on the changes in the electrical resistance caused by at least two consecutive processes of chemisorption, as shown in Figure 1—right. As gas sensors usually operate in the air atmosphere, the first process involves adsorption of oxygen according to the reaction proposed by Barsan and Weimar [31]:



where: $\text{O}_{\beta S}^{-\alpha}$ is a chemisorbed oxygen ion with: $\alpha = 1$ for singly ionized oxygen species, $\alpha = 2$ for doubly ionized oxygen species, $\beta = 1$ for atomic forms, $\beta = 2$ for molecular ions, S represents a surface site onto which oxygen can be adsorbed and e^- is an electron from the conduction band that is captured at the surface and provides the negative charge to the adsorbed oxygen ion. This leads to an overall increase in the sensor's resistance for n -type and a decrease for p -type semiconductors.

The second process of reaction of the reducing (CO) gases with the pre-adsorbed oxygen, described as [31]:



results in the opposite changes in the electrical resistance. Receptor function of a sensor, associated with electrical charge transfer processes, might be affected by the exposure of certain crystal facets. A detailed description of surface-controlled gas sensing processes can be found in Section 5.

It is worth noting that the facets of high surface energy may not be stable while they are exposed to the aggressive chemical compounds or undergo the thermal treatment [26]. Stability issue is very

important to such an extent that it seems necessary to perform in situ measurements or to apply the *operando* techniques in order to monitor the changes in the surface properties during photocatalysis and gas sensing [26].

There are many excellent reviews covering the topic of surface engineering and shape-controlled crystals in application to photocatalysis [5,27,32]. As far as gas sensing is concerned, this number is greatly reduced [8,9,33,34]. To the best of our knowledge, there are no such surveys treating at the same time both photocatalytic and gas sensing applications.

This review is mostly devoted to the following case-studies: TiO_2 —anatase, $\alpha\text{-Fe}_2\text{O}_3$ —hematite and Cu_2O . Their common feature is that they appear as good candidates for both photocatalysis and gas sensing.

2. Basic Properties of Chosen Metal Oxides

Basic properties of TiO_2 —anatase, $\alpha\text{-Fe}_2\text{O}_3$ —hematite and Cu_2O are listed in Table 1.

Titanium dioxide, TiO_2 crystallizes in three polymorphic forms: tetragonal anatase and rutile or orthorhombic brookite. Among them, the most thermodynamically stable and thus common in the environment is rutile. The other two polymorphic forms, namely anatase, and brookite are metastable and transform irreversibly into rutile upon heating [35,36]. Pure and stoichiometric titanium dioxide exhibits an insulating behavior at room temperature. In its non-stoichiometric form, TiO_2 represents an n-type semiconductor.

TiO_2 -anatase is a very unique material for photocatalysis and photoelectrochemical hydrogen generation. Its chemical stability and exceptional resistivity to corrosion and photocorrosion are well-known and widely-exploited features that could provide excellent performance in these applications. TiO_2 -anatase can be further characterized by non-toxicity, high transmittance for infrared radiation (the band gap of anatase is 3.2 eV), as well as excellent stability under reducing atmosphere. However, the electronic properties of TiO_2 such as a wide-bandgap and high electrical resistivity [36], create a serious obstacle from the practical point of view. Modification of both the band gap and the electrical conductivity is necessary to provide a better match to the light spectrum and improve current-voltage characteristics of photoanodes in the photoelectrochemical cells. The efficiency of the photocatalytic and photoelectrochemical processes is critically dependent upon the above-mentioned factors.

Microcrystalline TiO_2 is a bulk defect sensor working at very high temperatures (1000–1400 K). The gas sensing mechanism is governed by the thermodynamics of point defects such as doubly ionized oxygen vacancies and the equilibrium reactions between these point defects in the bulk and an oxygen partial pressure in the surrounding atmosphere. Recently, one can observe an increasing interest in modified nanosized TiO_2 for gas sensing. There is a big number of publications undertaking the issue of TiO_2 in a form of nanotubes [20,37,38], nanofibers [39], nanowires [21], and nanopowders [40,41] that exhibit promising gas sensing features.

Recently, the shape-controlled TiO_2 nanocrystals terminated with different crystal facets have been reported [9,15,25,42]. Naturally occurring TiO_2 nanocrystals expose low energy {101} facets. These crystallographic planes are characterized by the lowest surface energy of 0.49 Jm^{-2} related to the lowest atomic planar density of 5.1611 nm^{-2} and the lowest density of dangling bonds of 10.3222 nm^{-2} as compared to highly energetic {001} facets (see Table 1). It has been demonstrated that the activity of a facet is strongly dependent on the type of photocatalytic reactions and the related catalytic mechanisms. For example, the activity of anatase TiO_2 facets in degradation of dyes has been discovered to follow the order: {001} > {010} > {101} [43] while a different order {010} > {101} > {001} has been established for the photocatalytic H_2 evolution [44,45].

Iron (III) oxide has four polymorphs: $\alpha\text{-Fe}_2\text{O}_3$, $\beta\text{-Fe}_2\text{O}_3$, $\gamma\text{-Fe}_2\text{O}_3$, and $\epsilon\text{-Fe}_2\text{O}_3$ [46,47]. In nature, only $\alpha\text{-Fe}_2\text{O}_3$ and $\gamma\text{-Fe}_2\text{O}_3$ occur in a highly crystalline form. Known as hematite, $\alpha\text{-Fe}_2\text{O}_3$ is the most stable iron oxide under ambient atmosphere. Hematite crystallizes in the trigonal system consisting of iron atoms surrounded by six oxygen atoms in corundum arrangement (Table 1). Its moderate

band gap of about 2.2 eV corresponds to a visible range of the light spectrum which makes it a good candidate for water photodecomposition.

Table 1. Bulk and surface properties of TiO_2 , $\alpha\text{-Fe}_2\text{O}_3$, and Cu_2O .

Properties		TiO_2	$\alpha\text{-Fe}_2\text{O}_3$	Cu_2O
bulk	crystal lattice [24]	anatase	hematite	cuprite
	crystal system [24]	tetragonal	trigonal	cubic
	space group [24]	$I4_1/\text{amd}$ (141)	R-3C (167)	Pn-3 m (224)
	lattice parameters [24,48]	$a = b = 0.3785 \text{ nm}$ $c = 0.9513 \text{ nm}$ $\alpha = \beta = \gamma = 90^\circ$	$a = b = 0.5038 \text{ nm}$ $c = 1.3772 \text{ nm}$ $\alpha = \beta = 90^\circ$ $\gamma = 120^\circ$	$a = 0.4270 \text{ nm}$ $\alpha = \beta = \gamma = 90^\circ$
	cell volume [nm^3] [24,48]	0.1362	0.3027	0.0778
	the atomic separation [nm] [48–50]	Ti-O 0.194 O-O 0.279	Fe-O 0.194 Fe-Fe 0.290	Cu-O 0.184 O-O 0.368 Cu-Cu 3.01
	band gap [eV] [8,24]	3.2	2.2	2.2
	formula weight [gmol^{-1}]	79.9	159.7	143.1
	density [gcm^{-3}] [48,51,52]	3.79	5.24	5.75
	conductivity	n-type	n-type	p-type
	refractive index [53–55]	$n_{\text{ord}} = 2.5612$ $n_{\text{ext}} = 2.4880$ ($\lambda = 589.3 \text{ nm}$)	2.6580 ($\lambda = 2.5 \mu\text{m}$)	2.2620 ($\lambda = 2.5 \mu\text{m}$)
surface	surface energy [Jm^{-2}] [30,56–62]			
	(001)			
	(100)			
	(101)			
	(111)	0.98	1.53	
	(012)	0.58	1.37	1.194
	(104)	0.49	1.31	28.80
				0.677
			1.06	0.80
			1.45	
	atomic planar density [nm^{-2}] [8]			
	(001)			
	(100)			
	(101)			
	(110)			
	(111)	6.9821	4.5494	
	(113)		5.7651	10.997
	(012)	5.1611		
				7.7618
				6.3375
			7.3047	
			5.7651	
	dangling bonds density [nm^{-2}] [8]			
	(001)			
	(100)			
	(101)			
	(110)			
	(111)	20.9463	13.6482	
	(113)		11.5302	21.954
	(012)	10.3222		7.7618
				6.3375
			21.9147	
			17.3953	

Its low cost, abundance, environmental friendliness, high corrosion resistance, and excellent adhesion to the substrate contributes significantly to numerous applications, i.e., in photocatalytic degradation and electrode materials, heavy metal removal from the water/wastewater and water splitting. It has been used as a humidity sensor since the 1960s of the last century [63]. Generally, α -Fe₂O₃ shows n-type behavior because it has a tendency to become oxygen-deficient with oxygen vacancies. However, annealing in oxygen and the presence of cationic impurities result in a p-type conductivity. Various α -Fe₂O₃ nanomaterials such as nanoparticles [64,65], nanorods [66], nanowires [22], nanotubes [67], nanobelts [23], nanoflakes [68], nanodendrites, as well as solid and hollow spindles [69] have been successfully prepared.

The most frequently exposed {001} facet of α -Fe₂O₃, is terminated by Fe or O atoms only, whereas another low-index facet, {100}, contains both Fe and O atoms [70,71]. By using the solvothermal method, Lu and coworkers synthesized 27 nm-thick Fe₂O₃ nanodiscs bound by {001} facets [71]. By comparing the packing density of Fe³⁺ and O^{2−} for {001}, {100}, and {010} facets (Table 2), it could be clearly concluded that {001} facet exhibits the highest packing density of O^{2−} and that is why it is the most stable and the most exposed among other facets [69,71].

Table 2. Packing density of Fe³⁺ and O^{2−} for various facets of α -Fe₂O₃ nanodiscs [71].

	{100}	{010}	{001}
Fe ³⁺	2.89 nm ^{−2}	2.89 nm ^{−2}	9.11 nm ^{−2}
O ^{2−}	5.78 nm ^{−2}	5.78 nm ^{−2}	13.8 nm ^{−2}

Cuprous oxide (Cu₂O) crystallizes in a cubic crystal structure (space group of Pn3m) with a unit cell length of 0.4270 nm. Cu₂O is a nonstoichiometric, defect p-type semiconductor of a direct band gap of about 2.2 eV [8,24]. It is widely applied as an active element of catalytic oxidation of CO, water–gas shift reaction, CO hydrogenation reaction, partial oxidation of propylene, organic synthesis, photocatalysis, and photoelectrocatalysis [72].

In the studies of shape-controlled Cu₂O nanocrystals one can distinguish between three basic forms: cubes, octahedra, and rhombic dodecahedra, enclosed by the {100}, {111}, and {110} facets, respectively. All the surface Cu atoms are fully exposed in the case of {110} facets, while the {111} facet contains some exposed and some sub-surface Cu atoms. Only partially exposed Cu atoms are available in the case of the {100} facet of Cu₂O, which is also reflected in the experimental results, showing the low reactivity of {100}-facet bounded nanocubes. Performance of {111}-faceted octahedral Cu₂O nanoparticles surpasses largely that of other morphologically different Cu₂O nanoparticles [8].

Cuprous oxide Cu₂O can operate as a gas sensor at relatively low temperatures [73,74]. The conductivity of Cu₂O is mainly determined by the hole carrier density of the inter-granular contact region. The exposed crystal facets, size, and specific surface area of Cu₂O could play a significant role in gas sensing. So far, cuprous oxides of different shapes, e.g., flower-like [75], cubes [76], wires [77], concave [78] were investigated as benzene, NO₂, CO, and H₂S gas sensors [33,75–78]. It is worth noting that during H₂S detection, a reversible reaction between the cuprous oxide and hydrogen sulfide Cu₂S formation may occur. Due to the phase transformation, a highly electrical conductive path is being formed, thus enhancing the electrical conductance [79].

3. Growth and Morphology of Metal Oxide Nanocrystals

In the case of growth of nanomaterials both: the top-down and bottom-up strategies exist. The bottom-up strategy is the most appropriate when one considers the synthesis of size and shape-controlled metal oxide nanocrystals. Bottom-up synthesis of nanocrystals is quite a complex process that consists of two steps: nucleation and growth. The formation mechanism and shape evolution begin with the nucleation process, whereby nuclei act as seeds for the nanoparticle growth [24,80,81]. Within the classical nucleation theory, CNT, according to the definition given by Mullin [82], the nucleation is treated as a thermodynamic process driven by supersaturation of the bulk solution

and governed by the total free energy ΔG . Nucleation can be homogeneous when the nuclei are generated uniformly from the parent phase or heterogeneous if other material components may contribute to the process. In principle, the nucleation rate, subsequent aggregation/agglomeration, Ostwald ripening and other mechanisms occurring between the preformed nuclei, affect the size and number of growing nanoparticles. The thermodynamic and kinetic growth conditions, taking into account the temperature, pH of the solution, surfactants/capping agents, etc., determine their shape. However, it is extremely difficult to indicate the predominant role each of these processes play in the final morphology of metal oxide nanocrystals.

According to the classical nucleation theory, CNT, two processes take place simultaneously: (1) the surface reaction and (2) the monomers diffusion to the surface. Its main assumption is the existence of the critical radius, above which particles will form and grow.

Control of crystals morphology relies on many factors including its internal structure and the external growth conditions. Nevertheless, the final shape and growth direction are a consequence of the minimization of the surface energies.

Over the last several decades, with the development of particle synthesis methods, various theories regarding the growth pathways have been proposed. They can be divided into two categories: (a) diffusion and (b) aggregative growth [24,80,83].

The first one involves the following steps:

- diffusion of monomers to the surface, where they are adsorbed,
- surface reaction,
- byproducts desorption and diffusion into the bulk solution.

In this case, the following models can be distinguished: LaMer and Finke [80,84], Ostwald ripening [24,80], and interparticle growth [80].

Aggregative growth model describes the coalescence of initially formed primary particles and their following attachment [83]. The internal structure of as-formed particles can be random or ordered. Here, the following issues should be considered: evolution of the size distribution (formation of monodisperse polycrystalline colloids) and diffusion-limited or reaction-limited aggregation, where the rate of aggregation is affected by the rate of collisions due to the Brownian motion.

In order to enable evolution of particularly shaped nanocrystals, manipulation of the growth rate of certain facets is necessary. The following factors contributing to the shape manipulation have been reported [81]:

- reaction time,
- temperature,
- pressure,
- pH,
- concentration and type of capping agents (ions, surfactants, reducing agents, ligands, etc.).

The surface energy can be modified by the use of different methods of synthesis, reaction time or the nature of the surfactants [81,85]. Reaction temperature and pressure affect the rate of nucleation and growth of nanoparticles. Altering the pH affects the state of chemical species in the solution and coordination bonding with ions in the precursor. A solvent with the different functional groups provides various coordinations with the precursors. It is worth noting that nanocrystals can interact with each other by van der Waals forces [86] or by repulsive electrostatic interactions. Therefore, in order to prevent instability of the surface structure, the adsorption of surface ligands has been carried out. By adding the surfactants or additives, the surface tension is reduced. Capping agents or surface ions may prevent aggregation, which results in small particles formation.

Bottom-up strategy includes many methods such as physical (i.e., molecular beam epitaxy, evaporation) [87–89], wet-chemical (sol-gel, co-precipitation) [90–92], and hybrid route (i.e., sonochemical,

electrochemical) [93–95]. Among them, the sol-gel and solvothermal/ hydrothermal methods are the most widely used to tailor the shape-controlled crystals.

Sol-gel synthesis is one of the most-established methods to obtain metal oxide nanocrystals [90,96,97]. It is based on hydrolysis and polycondensation reactions involving mainly metal alkoxides $[M(OR)_3]$ as molecules to obtain oxides. The reaction pathway for the production of metal oxide in this method includes:

- solvolysis (hydrolysis or alcoholysis); production of the metal hydroxide solution described as a sol,
- condensation; formation of three-dimensional gels (metal–oxygen–metal interlocked network),
- drying process; depending on the mode of drying conversion to xerogel or aerogel

The nature of metal precursor and solvent plays a remarkable role in the synthesis of metal oxide nanocrystals. The aqueous sol-gel route is highly recommended for the synthesis of bulk metal oxides rather than their analogs in the form of nanomaterials. In this case, the synthesis steps (solvolysis, condensation, and drying) can undergo simultaneously, resulting in difficulty in controlling particle morphology. In a nonaqueous sol-gel process, organic solvents not only serve as oxygen suppliers but also offer a tool for tuning the morphology, surface properties, particle size, and composition of the final oxide material. For the fabrication of metal oxide nanocrystals, the surfactant-controlled strategy permits a control over the shape during their growth.

In the solvothermal method, the reactants are placed in an autoclave filled with water or organic compounds to carry out the reaction under high temperature and pressure conditions. If the nonaqueous solvents are utilized as the reaction medium, it is termed a “solvothermal method”; whereas when preparation is carried out in the presence of water, the term: “a hydrothermal process” is introduced. Typical steps in the solvothermal process are as follows: premixing, reaction and post-processing. Precise control of the hydrothermal/solvothermal process is the key factor that enables the synthesis of various nanostructured inorganic materials.

The most important factors affecting the obtained polyhedral crystals based on TiO_2 , Fe_2O_3 , and Cu_2O are collected in Tables 3–5 and described in Sections 3.1–3.3.

3.1. TiO_2 (Anatase)

Morphology and structure of TiO_2 nanoparticles can be effectively controlled by the surfactants as shown in Table 3.

In papers [25,42,98–102] the synthesis of TiO_2 nanocrystals with different shapes such as rods, cubes (truncated cubes), sheets, cuboids (truncated cuboid), octahedra (truncated octahedra), and bars by using a simple hydrothermal/solvothermal and wet-chemical route employing different capping agents has been demonstrated. Special surfactants that passivate the highly active facets are usually employed to direct the crystal growth.

Hydrofluoric acid was used as the first capping agent to obtain shape-controlled anatase nanocrystals with a high contribution of {001} planes [9,28,102,103]. Density functional theory (DFT) was used [25] to confirm that F^- ions constitute the best choice for decreasing the surface energy of {001} facets and make them more stable than {101} facets.

Hydrofluoric acid is an environmentally unfriendly and highly corrosive chemical. Recently, TiO_2 nanocrystals with the exposed reactive facets and different shapes have been synthesized by applying a fluorine-free strategy. The use of 1-butyl-3-methylimidazolium tetrafluoroborate ($[bmim][BF_4]$) as F^- source has also been extensively studied because it is more environmentally friendly than HF [101,104]. This ionic liquid plays a dual function: F^- ions stabilize {001} while $[bmim]^+$ capping on {100} facets provides TiO_2 nanocrystals in the shape of cuboids.

An interesting example of a fluorine-free strategy is the replacements of F^- ions by amines. In [98] it has been shown that the varying ratio of the bridging ligand (tetramethylammonium hydroxide (TBAH)) to capping agent (diethanolamine (DEA)) concentrations allows nanocrystals with different shapes to be obtained. When the bridging ligand concentration decreases, the morphology follows the

ellipsoids → rods → capsules → cuboids → sheets sequence. The hydrolysis rate of the precursor is determined by TBAH amount while DEA concentration is responsible for lowering the surface energy of {001} facets. We have recently reported [105] that the hydrothermal method based on the varying ratio of TBAH to DEA concentrations could be successfully applied to obtain TiO₂ nanocrystals of different shapes.

On the other hand, oleic acid and oleylamine (OLEA) surfactants are commonly used as capping agents in the shape-controlled synthesis. They have different binding strength to control the growth of the TiO₂ nanocrystals. Oleic acid, similarly to F[−] ions, stabilizes high energy {001} facets whereas OLEA capping promotes the growth of {101} facets. In the presence of water vapor, a simple variation of the oleic acid/OLEA molar ratio enables a fine control of the growth rate of TiO₂ nanocrystals [104].

A slightly different approach has been presented for obtaining nanobelts. As shown in Table 3, TiO₂ in the shape of nanowires was obtained as a first step by the hydrothermal method using commercial TiO₂ powder and NaOH solution. The next step was calcination of the precursor [106,107] or its hydrothermal synthesis to obtain nanobelts [43].

Table 3. Comparison of synthesis methods and application of various facet-dependent TiO₂.

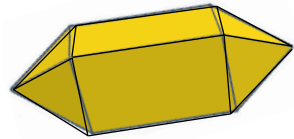
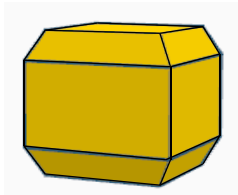
Synthesis Method	Ion Source	Other Reagents	Reaction Condition	Capping Agents	Ligand/(hkl)	Exposed Facets	Application	Ref.
rod								
hydrothermal	TTIP	DEA, TBAH	225 °C/24 h	DEA	DEA/(001)	(100) (101)	photocatalysis	[98]
	solution of TTIP in 2-propanol	TBAH, Me ₄ NOH	180 °C/10 h	-	-	(100) (101)	-	[99]
	ATNWs	H ₂ O	200 °C/24 h	CTAB	CTAB/(100)	(100) n/a	photocatalysis	[42]
	NaTNWs	H ₂ O	200 °C/24 h	OH ⁻	OH ⁻ /(100)	(100) n/a	promising photocatalyst	[100]
wet-chemical	TTIP	TMAO	80-100 °C/6-12 h	Oleic acid	n/a	n/a	-	[108]
truncated cube								
hydrothermal	TTIP	DEA, TBAH	225 °C/24 h	DEA	DEA/(001)	(101) (100) (001)	photocatalysis	[98]

Table 3. Cont.

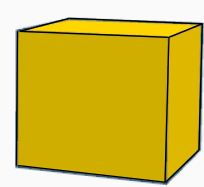
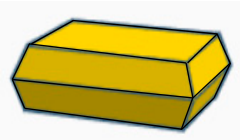
Synthesis Method	Ion Source	Other Reagents	Reaction Condition	Capping Agents	Ligand/(hkl)	Exposed Facets	Application	Ref.
cube								
hydrothermal	TBT	acetic acid, H ₂ O	180 °C/24 h	[bmin][BF ₄]	F [−] /(001) [bmim] ⁺ /(100)	(001) (100)	sodium ion battery anodes	[101]
	TBT	-	160 °C/20 h	OLEA, NH ₃ , HF	NH ₃ and HF/(111)	(101) (011) (111)	DSSC devices	[109]
	TiF ₄	H ₂ O ₂ , H ₂ O	180 °C/2 h	n/a	n/a	(001) n/a	photocatalysis	[110]
wet-chemical	TiCl ₄	H ₂ O	90 °C/4.5 h	CNC	n/a	n/a	—	[101]
sheet								
solvothermal	H ₂ O, acetic acid	[Na][BF ₄]	200 °C/24h	F [−] /(001)	H ₂ O, acetic acid	(001) (101)	promising photocatalyst	[104]

Table 3. Cont.

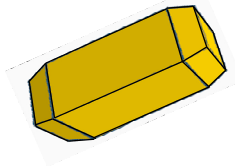
Synthesis Method	Ion Source	Other Reagents	Reaction Condition	Capping Agents	Ligand/(hkl)	Exposed Facets	Application	Ref.
hydrothermal	TTIP	TBAH	225 °C/24 h	DEA	DEA/(001)	(100) (001)	photocatalysis	[98]
	TiF ₄	H ₂ O	180 °C/20 h	HF	F [−] /(001)	(001) (101)	-	[25]
	TTIP	H ₂ O	180 °C/24 h	HF	F [−] /(001)	(001) (101)	photocatalysis	[102]
	TBOT	H ₂ O	180 °C/24 h	HF	F [−] /(001)	(001) (101)	gas sensors	[9]
	TTIP	H ₂ O	200 °C/24 h	HF	n/a	(001) (101)	photocatalysis	[28]
	TBOT	H ₂ O	180 °C/2 h	HF	F [−] /(001)	(001) (101)	H ₂ production	[103]
	TBOT	HCl, H ₂ O	150–180 °C /24 h	(NH ₄) ₂ TiF ₆	F [−] /(001)	(001) (101)	promising photocatalyst	[110]
	TiCl ₃	H ₂ O	180 °C/24 h	NH ₄ F	F [−] /(001)	(001) (101)	gas sensors	[111]
	TiCl ₃	NiCl ₂	180 °C/2 h	NH ₄ F	F [−] /(001)	(001) (101)	gas sensors	[112]
truncated cuboid								
hydrothermal	TTIP	DEA, TBAH	225 °C/24 h	DEA	DEA/(001)	(101) (100) (001)	photocatalysis	[98]
	solution of TTIP in 2-propanol	TBAH	180 °C/10 h	DVMT	Si-OH/(001)	(100) (001)	—	[99]

Table 3. Cont.

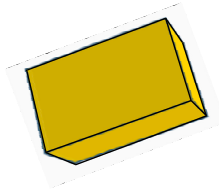
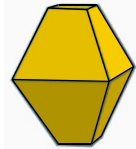
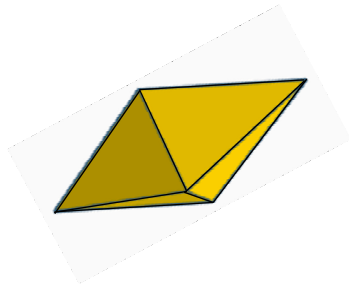
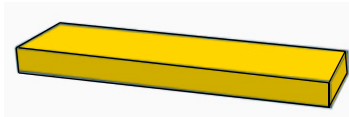
Synthesis Method	Ion Source	Other Reagents	Reaction Condition	Capping Agents	Ligand/(hkl)	Exposed Facets	Application	Ref.
cuboid								
hydrothermal	TiCl ₄	H ₂ O	160 °C/14 h	HCl, HF,	F [−] /(001) Cl [−] /(100)	(001) (100)	—	[113]
solvothermal	TTIP	acetic acid, H ₂ O	200 °C/24 h	[bmim][BF ₄]	F [−] /(001), [bmim] ⁺ /(100)	(001) (100)	promising photocatalyst	[104]
wet-chemical	TiCl ₄	ethanol, NH ₃	0 °C/5 h	-	n/a	n/a	photocatalysis	[114]
truncated octahedra								
wet-chemical	TiCl ₄	H ₂ O, n-heptane	100 °C/24 h	AOT	RSO ₃ [−] /(101)	(101) (001)	biomedical applications	[115]
hydrothermal	KTNWs	H ₂ O	200 °C/16 h	urea	CO ₃ ^{2−} /(001)	(101) (001)	photocatalysis	[116]
	TTIP	H ₂ O	160 °C/10 h	CH ₂ O ₂	CH ₂ O ₂ /(101)	(101) (001)	photocatalysis	[117]
	TBOT	ethanol	180 °C/18 h	Oleic acid, OLEA	Oleic acid/(001) OLEA/(101)	(101) (001)	-	[118]
	ATNWs	H ₂ O, NH ₄ F	200 °C/24 h	NH ₄ F	F [−] /(001)	(101) (001)	photocatalysis	[42]
	TBOT	oleic acid, NaF	250 °C/24 h	oleic acid, F [−]	F [−] /(001) oleic acid- n/a	(101) (001)	photocatalysis	[119]

Table 3. Cont.

Synthesis Method	Ion Source	Other Reagents	Reaction Condition	Capping Agents	Ligand/(hkl)	Exposed Facets	Application	Ref.
octahedra								
hydrothermal	KTNWs	H ₂ O	170 °C/4 h	-	-	(101)	photocatalysis DSSC devices	[43]
	KTNWs	H ₂ O	200 °C/16 h	NH ₄ Cl	NH ₄ ⁺ /n/a	(101)	photocatalysis	[116]
	TBOT	Oleic acid, OLEA, ethanol	180 °C/18 h	Oleic acid, OLEA	Oleic acid/(001) OLEA/(101)	(101)	-	[118]
belt								
hydrothermal	P25	NaOH	180 °C/24 h			(101)	gas sensors	[106]
	HTiO ₃	H ₂ O	170 °C/24 h			(010) (101)	photocatalysis DSSC devices	[43]
	TiO ₂ powder	NaOH	200 °C/24 h			(101)	photocatalysis	[107]

TBAH—tetramethylammonium hydroxide, TTIP—titanium(IV) isopropoxide, DVMT—the acid-delaminated vermiculite, KTNWs—K-titanate nanowires, TBOT—titanium butoxide, CTAB—hexadecyltrimethylammonium bromide, ATNWs—ammonium-exchanged titanate nanowires, PVA—polyvinyl alcohol, NaTNWs—Na-titanate nanowires, TBT—tetrabutyl titanate, AOT—Sodium bis(2-ethylhexyl) sulfosuccinate, P25—commercial TiO₂ powder, OLEA—Oleylamine, DSSC—Dye-Sensitized Solar Cell, TMAO—trimethylamino-N-oxide dihydrate, DEA—diethanolamine, PTA—peroxo titanic acid, CNC—cellulose nanocrystal, [bmin][BF₄][−]—1-butyl-3-methylimidazolium tetrafluoroborate.

3.2. α -Fe₂O₃ (Hematite)

The shape of nanocrystals based on hematite (α -Fe₂O₃) can be easily modeled because the lattice planes with low Miller indices have similar energy values. One of the possible ways of changing the morphology of α -Fe₂O₃ is to use the selective adsorption of ions (Table 4). During crystallization of this oxide, metal ions interact with the lattice planes of different atomic configuration, changing their surface energy. In literature, this process is known as metal-ion mediated route. The preferred direction of crystal growth of α -Fe₂O₃ can be changed by selection of the ions [120]. The selective adsorption of Zn²⁺ on the surface of the growing hematite determines the formation of cubes [120–123]. On the other hand, when Cu²⁺ ions are used, it is possible to obtain a rhombohedral and concave shape [122–124] whereas a plate structure can be fabricated by applying Al³⁺ ions [123,125]. Liu et al. [125] claimed that irrespective of the salt solution containing the appropriate ion, but under alkali condition, it is possible to obtain hexagonal nanoplates. Moreover, Al³⁺ ion will be mostly left in the solution. In our studies [126] it has been demonstrated that the application of Zn²⁺ and Al³⁺ to the ion-mediated hydrothermal route is the reason for the formation of α -Fe₂O₃ with cubic and disc structures, respectively. However, the incorporation of ions into the crystal lattice of nanocrystals is observed. Therefore, using this technique one should take into account the effect of the phase composition on the properties of the obtained materials.

On the other hand, the presence of the specific ligands or surfactants also affects the growth of nanomaterials with well-defined facets. The most typical ligands are OLEA and OA (oleic acid) [127–129]. The first one is responsible for stabilization of nanocrystals, while the second by selective adsorption on {104} planes affects reduction of the surface energy and directed crystal growth. The whole process of crystal growth under these conditions may be attributed to the aggregation and Ostwald ripening. Moreover, Rashid et al. [128] claim that oleate anions as capping agents inhibit the formation of Fe-O-Fe bonds due to the strong covalent interaction between them and Fe³⁺.

Gao et al. [121] compared the above-mentioned techniques: the metal-ion mediated route and application of surfactants/capping agents (hydrazine (N₂H₄) and carboxymethyl cellulose). It was found out that N₂H₄ had the ability to reduce iron oxidation state from 3+ to 2+, so in the solution, an additional “free” ion was present and acted in a similar way as Ni²⁺ or Zn²⁺ did.

Table 4. Comparison of synthesis methods and application of various facet-dependent α -Fe₂O₃.


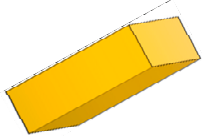
Synthesis Method	Ion Source	Ion Additive	Exposed Facets	Reaction Condition	Application	Ref.
hydrothermal	cube					
	Fe(C ₂ H ₂ O ₂) ₂	-	{102} {012} {112}	180 °C/2 h	photocatalytic degradation of RhB	[127]
	FeCl ₃ *6H ₂ O	-	{102} {012} {112}	180 °C/4–12 h	can be used for magnetic properties	[128]
	K ₃ [Fe(CN) ₆]	Ni ²⁺ , Zn ²⁺	{012} {10–2} {1–12}	160 °C/6 h	-	[121]
	Fe(NO ₃) ₃	Zn ²⁺	{014} {104}	160 °C/16 h	lithium-ion batteries	[122]
	Fe(NO ₃) ₃ *9H ₂ O	Zn ²⁺	{104} {–1–10}	160 °C/16 h	magnetic properties	[120]
	FeCl ₃ *6H ₂ O	-	n/a	160 °C/24 h	photocatalytic degradation of RhB	[130]
	Fe(NO ₃) ₃ *9H ₂ O	Zn ²⁺	{012}	160 °C/6 h	photocatalytic degradation of RhB	[123]
	Fe(NO ₃) ₃ *9H ₂ O	Na ⁺	{102} {104}	200 °C/24 h	photocatalytic O ₂ evolution	[32]
cuboid						

Table 4. Cont.

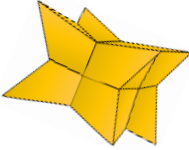
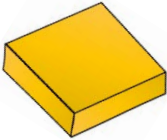
Synthesis Method	Ion Source	Ion Additive	Exposed Facets	Reaction Condition	Application	Ref.
hydrothermal	FeCl ₃ *6H ₂ O	-	{010} {001}	180 °C/4 h	lithium-ion batteries	[131]
thorhombic						
hydrothermal	Fe(NO ₃) ₃	Cu ²⁺	{−102} {012}	160 °C/16 h	lithium ion batteries	[122]
	Fe(NO ₃) ₃ *9H ₂ O	Cu ²⁺	{−102} {012}	160 °C/16 h	magnetic properties	[120]
	Fe(NO ₃) ₃ *9H ₂ O	Cu ²⁺	{104}	160 °C/6 h	photocatalytic degradation of RhB	[123]
polyhedron						
hydrothermal	FeCl ₃ *6H ₂ O	-	{104}	120 °C/12 h	humidity sensors	[132]
	Fe(acac) ₃	Na ⁺	{012}	180 °C/24 h	CO conversion, acetone and methanol sensing	[129]
	K ₃ [Fe(CN) ₆]	Cu ²⁺	{104}	160 °C/6 h	-	[133]
	FeCl ₃ *6H ₂ O	-	{104}	180 °C/8 h	lithium storage	[133]
	FeCl ₃	Na ⁺	{100} {011} {111}	200–230 °C/0.5 h	potentially exhibits good properties in future gas sensor	[134]

Table 4. Cont.

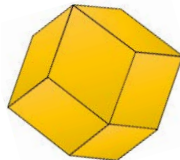
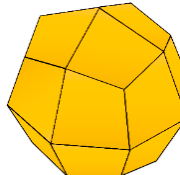
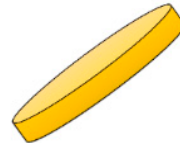

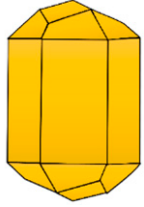
rhombohedron						
hydrothermal	$\text{FeCl}_3 \cdot 6\text{H}_2\text{O}$	-	{104}	220 °C/24 h	electrochemical sensor for H_2O_2	[135]
	$\text{FeCl}_3 \cdot 6\text{H}_2\text{O}$	-	{104}	150 °C/75 min	lithium storage	[136]
octahedron						
microwave assisted	$\text{FeCl}_3 \cdot 6\text{H}_2\text{O}$	-	n/a	150 °C/2 h	lithium storage	[93]
hydrothermal	FeCl_3	Na^+	{012} {104}	220 °C/48 h	photocatalytic O_2 evolution	[32]
	$\text{FeCl}_3 \cdot 6\text{H}_2\text{O}$	-	{104} {112}	220° C/24 h	electrochemical sensor for H_2O_2	[137]
plate						

Table 4. Cont.

hydrothermal	$\text{Fe}(\text{acac})_3$	-	$\{001\}$ $\{012\}$	180 °C/24 h	CO conversion, acetone and methanol sensing	[129]
	$\text{FeCl}_3 \cdot 6\text{H}_2\text{O}$	Na^+	$\{001\}$	200 °C/22 h	lithium-ion batteries	[131]
	$\text{Fe}(\text{NO}_3)_3 \cdot 9\text{H}_2\text{O}$	Al^{3+}	$\{110\}$	160 °C/6 h	photocatalytic degradation of RhB	[123]
	$\text{Fe}(\text{NO}_3)_3$	Al^{3+}	$\{001\}$	160 °C/16 h	magnetic properties	[125]
	FeCl_3	Na^+	n/a	140 °C–200 °C/0.5 h	photocatalytic degradation of MB	[94]
concave						
hydrothermal	$\text{Fe}(\text{NO}_3)_3$	Cu^{2+}	$\{13-44\}$ $\{12-38\}$	at 140 °C for 16 h	catalytic activity and high stability for CO oxidation	[124]
icositetrahedron						
hydrothermal	$\text{FeCl}_3 \cdot 9\text{H}_2\text{O}$	Na^+	$\{113\}$ $\{110\}$	22 °C/5 h	photocatalytic degradation of RhB	[138]

RhB—Rhodamine B, MB—methylene blue, $\text{Fe}(\text{acac})_3$ —iron (III) acetylacetonate.

3.3. Cu₂O

In contrast to TiO₂ and Fe₂O₃ facet-dependent nanocrystals, variously shaped copper oxide materials can be synthesized in a simpler way (Table 5). The most widely used technique to control the exposed facets is a wet-chemical route carried out at moderate temperature (approximately 55°/60 °C) for a short period of time (from 5 to 120 min) [18,138,139]. Nevertheless, capping reagent applied to the solution system is a crucial factor.

The presence of sulfosuccinate ions (AOT) [16] in solution affects crystal growth along <111> direction. It is possible that negatively charged oxygen atoms in the AOT interact with positively charged copper ions along <111> direction. A strong reducing agent like hydrazine (N₂H₂) [138,140] promotes generation of a big number of nuclei. With a small addition of N₂H₂ (approximately 0.1 mL) the cubic form becomes favorable, however, when the amount of hydrazine increases to 2.8 mL, the octahedral shapes are formed [138]. Polyvinyl pyrrolidone, PVP adsorbs at high index facets such as {111} [76,141,142]. Truncated octahedra composed of eight {111} planes and six {100} facets can be obtained when the concentration of PVP is moderate (1.5 mM). With the increasing amount of PVP during synthesis, the area ratio of {111} and {100} exposed facets increases, to reach finally an octahedral structure (PVP~4.5 mM). This is due to the strong interaction between the oxygen and/or nitrogen atoms of PVP and {111} facets. In many papers, the use of sodium dodecyl sulfate (SDS) as a capping reagent has been reported [138,143–146], however the mechanism of its selective adsorption is unclear. Its properties are supposed to be similar to those of AOT [147]. New possibilities in Cu₂O structure formation appear with the use of KBr. Liu et al. [148] demonstrated that the bromide ions can adsorb on {100} crystals facets and reduce their surface energy.

On the other hand, copper can easily undergo redox reaction and change its oxidation state according to the:



Therefore, to obtain a specific form, a reducing agent is used, the most popular being: glucose [139–141,149], ascorbic acid (AA) [16,76,142,150] and hydroxylamine hydrochloride (NH₂OH·HCl) [138,143,144] or hydrazine [90].

However, more complex morphologies are expected by controlling the experimental parameters such as temperature and pressure [16,76,144].

Table 5. Comparison of synthesis methods and application of various facet-dependent Cu₂O.

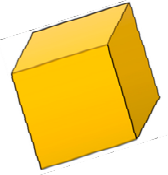
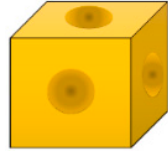
Synthesis Method	Ion Source	Reaction Condition	Capping Reagent/ Reducing Agent	Application	Ref.
wet-chemical	cube				
	CuCl ₂ ·2H ₂ O	30 °C/30 min	PVP/AA	lithium-ion batteries	[150]
	Cu(Ac) ₂	50 °C/30 min	N ₂ H ₄ /N ₂ H ₄	<ul style="list-style-type: none"> clock reactions should enhance the efficiency of organocatalytic and photocatalytic reactions 	[138]
	CuCl ₂	30–32 °C/1 h	SDS/NH ₂ OH·HCl	catalyzed click reactions	[146]
	CuSO ₄	80 °C/2 h	PVP/glucose	—	[141]
	CuSO ₄	70 °C/6–7 min	N ₂ H ₄ /glucose	clock reactions, catalytic activity	[140]
	CuSO ₄	55 °C/1 h	EDTA/glucose	nonenzymatic glucose sensor	[139]
	CuCl ₂	32–34 °C/1 h	SDS/NH ₄ OH·HCl	can be used as catalyst and hosts for nanostructure encapsulation	[143]
hydrothermally	Cu(Ac) ₂	80 °C/2 h	AOT/AA	photocatalytic H ₂ evaluation—methanol decomposition	[16]
	CuCl ₂ ·2H ₂ O		SDS/NH ₄ OH·HCl	biosensor (H ₂ O ₂)	[144]
	CuCl ₂ ·2H ₂ O	150 °C/12 h	PVP/AA	CO gas sensing	[76]
concave cubes					

Table 5. Cont.

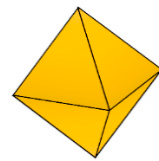
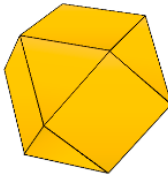
Synthesis Method	Ion Source	Reaction Condition	Capping Reagent/ Reducing Agent	Application	Ref.
hydrothermally	Cu(Ac) ₂	80 °C/2 h	AOT/AA	photocatalytic H ₂ evaluation— methanol decomposition	[16]
octahedron					
wet-chemical	CuCl ₂	RT/5–60 min	PVP/N ₂ H ₄	photocatalytic degradation of methylene orange	[90]
	CuCl ₂ ·2H ₂ O	30 °C/30 min	PVP/AA	lithium-ion batteries	[150]
	CuCl ₂	50 °C/30 min	N ₂ H ₄ /N ₂ H ₄	<ul style="list-style-type: none"> • clock reactions; • should enhance the efficiency of organocatalytic and photocatalytic reactions 	[138]
	CuCl ₂	30–32 °C/2 h	SDS/NH ₂ OH·HCl	catalyzed click reactions	[146]
	CuCl ₂	30 °C/20 min	PVP/AA	gas sensing	[33]
	Cu(NO ₃) ₂		ammonia/-	photocatalytic activity	[151]
hydrothermally	Cu(Ac) ₂	at 140 °C for 24 h	glycine/-	bacterial activity	[91]
	CuCl ₂ ·2H ₂ O		SDS/NH ₂ OH·HCl	biosensor (H ₂ O ₂)	[144]
cuboctahedron					

Table 5. Cont.

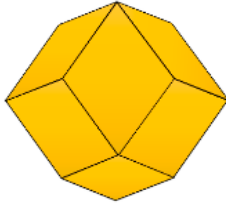
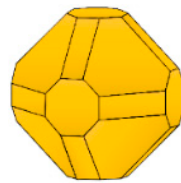
Synthesis Method	Ion Source	Reaction Condition	Capping Reagent/ Reducing Agent	Application	Ref.
wet-chemical	CuCl ₂	RT/5–60 min	PVP/N ₂ H ₄	photocatalytic degradation	[90]
	CuCl ₂ ·2H ₂ O	55 °C/3 h	PVP/-	<ul style="list-style-type: none"> • photocatalytic degradation of RhB • H₂ evolution reactions 	[18]
rhombic dodecahedron					
wet-chemical	CuCl ₂		SDS/NH ₂ OH·HCl	<ul style="list-style-type: none"> • drug delivery • molecular sensing 	[145]
	CuCl ₂	30–32 °C/1 h	SDS/NH ₂ OH·HCl	catalyzed click reactions	[146]
hydrothermally	CuCl ₂ ·2H ₂ O		SDS/NH ₂ OH·HCl	biosensor (H ₂ O ₂)	[144]
facet-selective etching	CuCl ₂	32–34 °C/1 h	SDS/NH ₂ OH·HCl	use as catalyst and hosts for nanostructure encapsulation	[143]
truncated octahedra					
hydrothermally	Cu(NO ₃) ₂		ammonia/-	photocatalytic activity	[151]

Table 5. Cont.

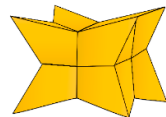
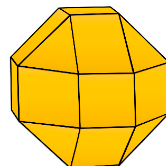

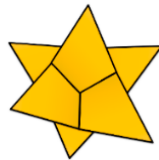
Synthesis Method	Ion Source	Reaction Condition	Capping Reagent/ Reducing Agent	Application	Ref.
wet-chemical	$\text{CuCl}_2 \cdot 2\text{H}_2\text{O}$	1–10 h/75 °C	-/glucose	<ul style="list-style-type: none"> potential application in solar energy conversion, catalysis as a model system for fundamental research 	[149]
	CuSO_4	80 °C/2 h			[141]
octopod					
wet-chemical	$\text{Cu}(\text{Ac})_2$	80 °C/2 h	AOT/AA	<ul style="list-style-type: none"> photocatalytic hydrogen evolution methanol decomposition 	[16]
	$\text{Cu}(\text{Ac})_2$	32–34 °C/2 h	SDS/ $\text{NH}_2\text{OH} \cdot \text{HCl}$	<ul style="list-style-type: none"> clock reactions should enhance the efficiency of organocatalytic and photocatalytic reactions 	[138]
polyhedron					

Table 5. Cont.


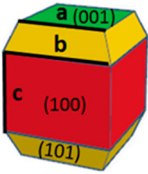
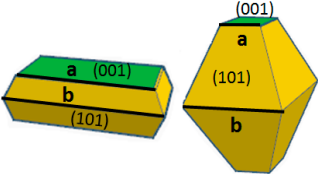
Synthesis Method	Ion Source	Reaction Condition	Capping Reagent/ Reducing Agent	Application	Ref.
wet-chemical	$\text{CuCl}_2 \cdot 2\text{H}_2\text{O}$	55 °C/3 h	PVP/AA	photocatalytic activity on the decomposition of methylene orange	[142]
	$\text{Cu}(\text{Ac})_2$	150 °C/12 h	N_2H_4 /glucose	<ul style="list-style-type: none"> degradation of organic pollutants photodecomposition of methylene orange 	[152]
star-shaped/extended hexapod					
wet-chemical	CuSO_4	80 °C/2 h	PVP/glucose		[141]
	$\text{CuSO}_4 \cdot 5\text{H}_2\text{O}$	80 °C/15 min	KBr/glucose and trisodium citrate	non-enzymatic sensor	[148]
hydrothermally	$\text{CuCl}_2 \cdot 2\text{H}_2\text{O}$		SDS/ $\text{NH}_2\text{OH} \cdot \text{HCl}$	biosensor (H_2O_2)	[144]
concave octahedral					
wet-chemical	CuCl_2	RT/2 h	SDS/ $\text{NH}_2\text{OH} \cdot \text{HCl}$	benzene and nitrogen dioxide sensing	[78]

PVP—poly (vinyl pyrrolidone), AA—ascorbic acid, SDS—sodium dodecyl sulfate, AOT—sulfosuccinate ions, EDTA—ethylenediaminetetraacetic acid.

3.4. Geometrical Considerations

For differently shaped nanocrystals it is possible to predict theoretically the contribution of the exposed facets corresponding to particular forms. This very useful approach is based totally on geometrical considerations as shown in Table 6 for TiO₂.

Table 6. Formulas enabling calculations of the percentage of exposed facets.

Shape	Theoretical % of Exposed Facets	Scheme
rod [98]	$S_{\{100\}} \% = \frac{c}{c+h} \cdot 100\%$ $S_{\{101\}} \% = 100\% - S_{\{100\}} \%$	
truncated cube [98]	$S_{\{001\}} \% = \frac{\cos\theta}{\cos\theta + \left(\frac{b}{a}\right)^2 + 2 \cdot \frac{b \cdot c}{a^2} \cdot \cos\theta - 1} \cdot 100\%$ $S_{\{100\}} \% = \frac{2c \cdot \cos\theta}{2c \cdot \cos\theta + b + \frac{a^2}{b} (\cos\theta - 1)} \cdot 100\%$ $S_{\{101\}} \% = 100\% - S_{\{001\}} - S_{\{100\}}$	
sheet/truncated bipyramid [1]	$S_{\{001\}} = \frac{\cos\theta}{\cos\theta + \left(\frac{b}{a}\right)^2 - 1} \cdot 100\%$ $S_{\{101\}} \% = 100\% - S_{\{001\}}$	

¹ θ —Theoretical value for the angle between the {001} and {101} facets of anatase equal to 68.3°.

The geometrical model of anatase TiO₂ single crystal developed by Yu and co-workers [1] enables to calculate the percentage of exposed {101} and {001} facets for nanocrystals in a form of sheet and truncated bipyramid. The percentage of the exposed facets for rod and truncated cube nanocrystals was also determined by similar geometrical models proposed by Roy et al. [98]. The average a, b, c, and h values can be evaluated by measuring the size of particles in TEM or SEM images while θ is the theoretical value for the angle between the {001} and {101} facets of anatase. Formulas enabling calculations of the percentage of exposed facets are included in Table 6.

Experimental verification of the geometrical models can be done, e.g., by Raman spectroscopy as proposed by Tian et al. [153] for anatase TiO₂. Based on the relationship between the intensities of Raman vibrational modes E_g and A_{1g} the percentage of {001} facets can be calculated. The E_g mode is assigned to the symmetric stretching vibrations of O-Ti-O, while A_{1g} is caused by asymmetric bending of O-Ti-O. Decreased intensity of E_g Raman mode and increased intensity of A_{1g} signifies higher percentage of {001} facets being exposed.

For other metal oxides such as Cu₂O, the ratio of the growth rates of {100} to {111} planes can be systematically increased as indicated by the following formula:

$$R = \frac{V_{\{100\}}}{V_{\{111\}}} = \frac{a}{b} = \frac{h \cos\theta}{h \sin(\theta + \alpha)} = \frac{\cos\theta}{\sin(\theta + \alpha)} = \frac{\cos\theta}{\sin(\theta + 32.25^\circ)} \quad (4)$$

The R parameter given by Equation (4) was calculated based on Figure 2a,b [154].

The theoretical value of angle α is 32.25° and θ is variable. For $\theta = 0^\circ$, the calculated R is 1.73, what corresponds to the octahedron shape, while for $\theta = 90^\circ$ (cube structure) R = 0.58 [155]. This method makes it possible to design particular polyhedral architectures.

The above geometric model has been verified experimentally by Zhang et al. [156]. It was found that the increasing amount of PVP, despite the fact it is claimed to be non-ionic, affects the final shape.

By selective adsorption of PVP on high index facets {111} the shape evolution of the Cu_2O nanocrystals in particular direction was reported (Figure 3).

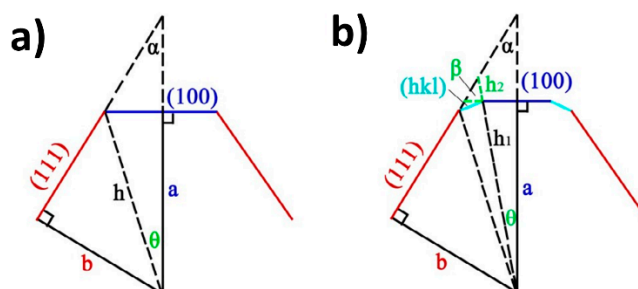


Figure 2. Geometrical construction for prediction of ratio of {111} and {100} index facets. The red and blue lines are assigned to the {111} and {100} facets, respectively, and cyan represents {hkl} plane. (a) Only low index facets and (b): both low and high indexed facets Reprinted with permission from ref. [154].

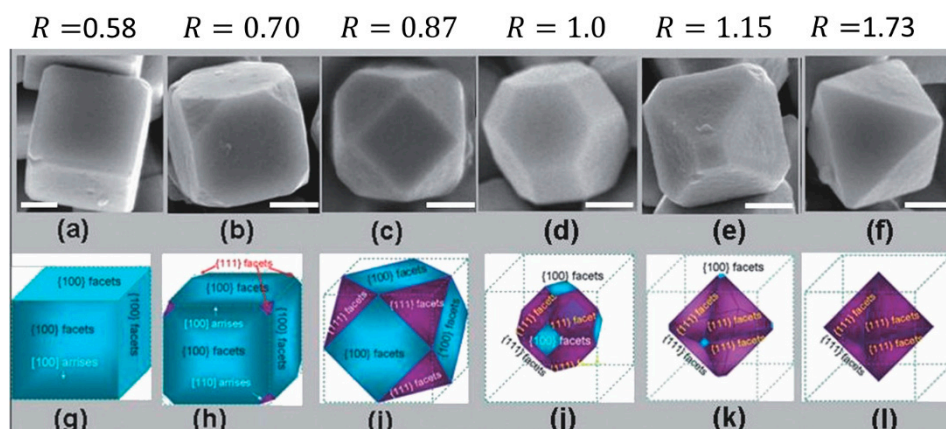
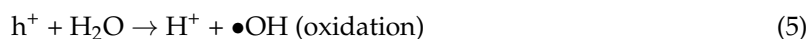


Figure 3. FESEM images of Cu_2O polyhedrons with different volume ratio R of {100} to {111} where (a) $R = 0.58$, (b) $R = 0.70$, (c) $R = 0.87$, (d) $R = 1.0$, (e) $R = 1.15$, (f) $R = 1.73$ with corresponding geometry 3D models (g–l). Reprinted with permission from ref. [156].

4. Photocatalytic Activity

In a typical photocatalytic process, fast generation and transfer of charge carriers to the reaction sites play an important role in the conversion of solar to chemical energy. The photocatalytic activity depends on the ability of the catalyst to generate electron-hole pairs, which, after separation into individual electric charges, participate in redox reactions, e.g.,



The resulting free radicals, such as $\bullet\text{OH}$ and $\text{O}_2\bullet^-$ are very active in secondary reactions, leading to, among others, decomposition of organic molecules [157,158]. It has been demonstrated recently [44,159] that particular design of interfaces and surfaces in shape controlled micro/nanocrystals can significantly improve the photocatalytic performance. The most direct effect of the exposed facets is related to the dangling bonds and low-coordinated atoms at terraces, steps, kinks, adatoms, and vacancies [5].

As shown in Figure 4, the mechanism of photocatalysis of facet-engineered surfaces and interfaces is largely affected by the following steps:

- I. electron e^- and hole h^+ excitation into the corresponding conduction CB and valence VB bands on particular crystal facets

- II. transport and separation resulting in accumulation of photogenerated charge carriers on different facets
- III. adsorption and activation of reactant molecules on facets with a different arrangement of atoms
- IV. charge transfer to different facets where particular molecules are adsorbed
- V. tunable efficiency of redox reactions.

As far as step I is being considered, the surface facets of semiconductors may possess different electronic band structures, caused by their atomic arrangements. The shift of CB and VB energy levels by surface states would allow for better adaptation to the reduction and oxidation potentials of photogenerated carriers, respectively.

Step II is involved in the dependence of charge transfer and separation on crystal orientation driven by the internal electric field.

In step III, the structural features affect the adsorption and activation of the reactant molecules, varying photocatalytic activity, and selectivity. Selectivity of the photocatalytic processes is also provided by the charge transfer to different facets where particular molecules are adsorbed (step IV).

Finally, in step V one can take advantage of differences in surface electronic band structures for various facets thus tuning the redox capabilities to particular processes [160].

Such tuning abilities have been demonstrated for certain metal oxides such as SnO_2 , WO_3 and Bi_2O_3 that suffer from too low energy of the conduction band minimum [161]. The upward shift of CB provided by {002} facets in the case of WO_3 , allows to fulfill the condition $E_{\text{CB}} > E_{\text{RED}}$ for hydrogen evolution process to take place [162].

When additives are used to control the growth process, it is very important that obtained materials were of high purity, which provides a significant amount of active sites necessary for the redox reaction. Therefore, the surfactant used should be characterized by easy solubility and degradability during or immediately after synthesis (washing with solutions of a specified composition and pH or annealing at elevated temperatures). For example, Chanda et al. [148] used an ethanol solution to remove SDS. To confirm the removal of adsorbed species from the surfaces, Fourier transform infrared spectroscopy (FTIR) measurements were performed before and after washing. The absence of the bands assigned to organic compounds of capping reagent proves cleaning efficiency. On the other hand, Jiang et al. [163] elevated temperature to about 400 °C, not only to crystallize the material but also to completely remove the residues of the tetramethylammonium hydroxide (TMAH) additive.

It is worth noting that during synthesis some ions from the capping agent can be embedded in the crystal network of the material, so they cannot be removed [120,125]. Therefore, the influence of the doping agent should be taken into photocatalytic activity consideration.

In conclusion, increasing the percentage of active crystallographic facets helps to develop highly efficient photocatalytic materials based on the following metal oxide micro- and nanocrystals: SnO_2 [163], WO_3 [162,164], Bi_2O_3 [165,166], BiVO_4 [167,168], anatase TiO_2 [15,28,42,98,99,102], $\alpha\text{-Fe}_2\text{O}_3$ [32,123,124], and Cu_2O [16,18,72,90]. Nevertheless, a synergetic effect of various surfaces of semiconducting crystals has been exploited as well.

Examples of improved photocatalytic performance are given below for TiO_2 —anatase, $\alpha\text{-Fe}_2\text{O}_3$ —hematite and Cu_2O .

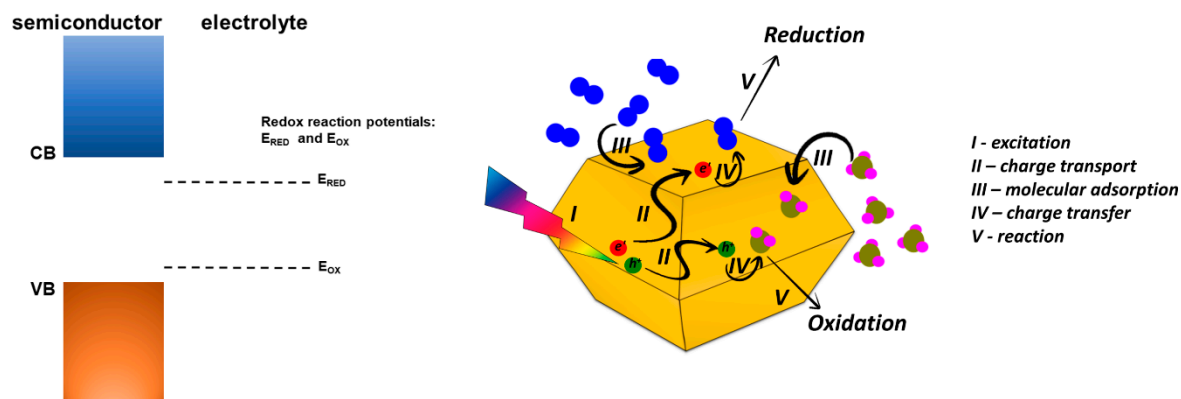


Figure 4. Schematic illustration of photocatalytic processes with facet-dependent photogenerated charge separation.

4.1. TiO_2 (Anatase)

The studies of facet-dependent photocatalytic activity of TiO_2 —anatase date back to 2008 when it has been established by Yang et al. [25] that the crystals with dominant {001} facet in general exhibit higher reactivity as compared to {101} ones. This phenomenon has been initially explained by theoretical simulations of the behavior of low coordination $Ti5c$ centers that at high concentration, increase the surface energy. The example of synergy of the coexisting two facets {101} and {001} has been demonstrated experimentally [45,169,170]. This effect has been attributed to an efficient charge separation, i.e., electrons transfer to {101} facets while holes—to {001} facets [171]. Ye et al. [111] prepared two crystals: one containing two facets {101} and {001} while in the second one {101} was replaced by {010}. This replacement resulted in a dramatic deterioration of both oxidation and reduction photocatalytic activities as shown in Figure 5a,b attributed to the inhibition of electron-hole separation. Direct proof of the increased recombination rate has been obtained from the photoluminescence PL signal associated with 2-hydroxy terephthalic acid (TAOH) from the reaction of terephthalic acid (TA) with $\bullet OH$ (Figure 5a) and transformation percentage of nitroblue tetrazolium (NBT) from the reaction of NBT with $O_2\bullet^-$ (Figure 5b).

The influence of the percentage of highly reactive facets on the photocatalytic activity of TiO_2 anatase crystals has been studied by Roy et al. [98] and on the hydrogen production—by Liu et al. [15]. Figure 5c illustrates how the degradation rate of methyl orange MO and methylene blue MB depend on the shape of TiO_2 —anatase nanocrystals. Figure 5d relates the shape of nanocrystals to the real contribution of {100}, {001} and {101} facets. The synergetic effect of the coexistence of low {101} and high energy {100} facets manifests itself in the highest photodegradation rate of both MO and MB by nanorods with 25% of {101} and 75% of {100}. Nanosheets dominated by high energy {001} and {100} facets, 72% and 28%, respectively and nanoellipsoids enclosed totally by low energy {101} facets demonstrate the lowest photoactivity towards decomposition of MO and MB dyes. From the experiments performed by Liu et al. [15], it could be concluded that the optimum ratio of the oxidative {001} to the reductive {101} facets existed for hydrogen evolution, as shown in Figure 5e. The truncated tetragonal bipyramids of TiO_2 anatase with 14.9% of {001} facets demonstrated the best photocatalytic activity for H_2 generation, whereas the octahedral crystals terminated with {101} facets appeared as completely inactive. The dependence of the photocatalytic activity on the percentage of the exposed facets has been attributed to the electron-hole recombination rate.

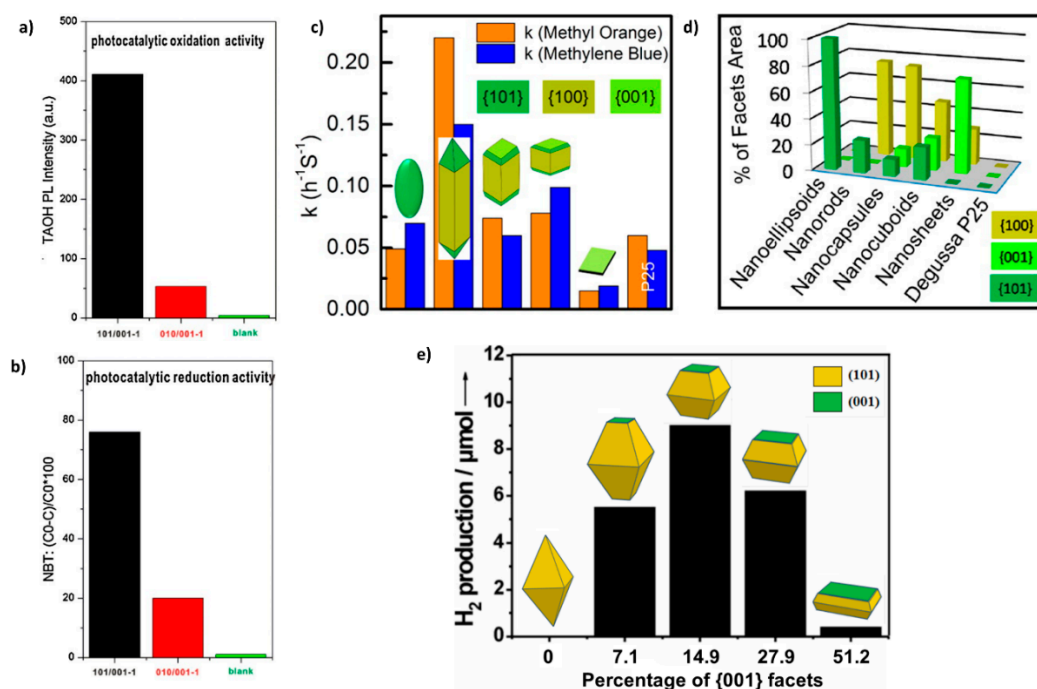


Figure 5. The intensity of PL signal associated with the reaction of TA (terephthalic acid) with $\bullet\text{OH}$ resulting in the formation of TAOH (2-hydroxy terephthalic acid) (a), the percentage of reduced NBT (nitroblue tetrazolium) from the reaction of NBC with $\text{O}_2^{\bullet-}$ (b). Reprinted with permission from ref. [111]. Dependence of the rate constant of MO and MB degradation on different shapes of TiO₂ nanocrystals (c), relative % of exposed facets area for the examined shapes (d). Reprinted with permission from ref. [98]. Photocatalytic H₂ production using TiO₂ nanocrystals with different amount of highly reactive {001} facets after 6 h irradiation (e). Reprinted and modified with permission from ref. [15].

4.2. $\alpha\text{-Fe}_2\text{O}_3$ (Hematite)

Among all iron oxides, hematite is well known for its catalytic properties enabling to conduct efficiently the catalytic oxidation of CO to CO₂ [172,173]. It is believed [174] that even under the extra-terrestrial conditions, i.e., in hot, CO₂-rich planetary atmospheres, such as Venus, oxidation of gaseous CO occurs on the surface of the mineral hematite Fe₂O₃.

Carbon monoxide is an odorless, colorless and extremely toxic gas. It is generally produced and released from the partial combustion process of fossil fuels, in many industrial processes and especially in the automotive exhaust systems. Its quick removal from the atmosphere by catalytic oxidation to CO₂ is required for the safety reasons. Another important application can be found in fuel cells, alternative for conventional internal combustion engines, where the hydrogen-rich gas mixture obtained by the partial oxidation or steam reforming of a hydrocarbon fuel usually contains byproducts, mainly carbon monoxide. Even a small amount of CO present in the reformed gas mixture may poison the electrodes of the fuel cell, therefore selective catalytic oxidation of CO to CO₂ has been found to be the most effective way to remove the trace amounts of CO from hydrogen.

Facet-dependent reactivity of Fe₂O₃ single crystals has been studied in relation to catalysis [175–178]. Recent studies of the shape-controlled nanocrystals for CO catalytic conversion to CO₂ by Ouyang et al. [129], Liang et al. [124] and Sun et al. [175] demonstrate that not only the specific surface area SSA plays an important role in this process but morphology and high Miller index planes exposed to the gas atmosphere contribute as well. Figure 6a presents the influence of temperature on the progress in CO conversion for $\alpha\text{-Fe}_2\text{O}_3$ micro/nanocrystals along with the mechanism proposed by Sun et al. [175].

Sun et al. [175] synthesized plate, cube and rod microcrystals of $\alpha\text{-Fe}_2\text{O}_3$ by different hydrothermal methods and discussed the effect of morphology on the CO catalytic activity. These authors demonstrated the onset of the conversion process at about 120 °C for rods enclosed within {110}

planes and, as a consequence, the best conversion efficiency at each reaction temperature studied. At 160 °C, CO conversion amounted to 21.7% for rods with {110} facet exposed, 9% for cubes with {012} facets exposed and 0 for plates with {001} facet exposed. The CO activities follow the order of: rods with {110} > cubes with {012} > plates with {001}. It should be mentioned however that this order does not match the surface energy sequence corresponding to these planes (see Table 1). It reflects the fact that planes of low Miller indices have almost the same surface energy in the case of α -Fe₂O₃. The catalytic activity does not scale with the SSA either as 6.352 m²g^{−1} was obtained for rods, 1.835 m²g^{−1} for cubes, and 31.533 m²g^{−1} for plates.

The effect of increased activity for rods has been accounted for [175] by assuming different abilities of chemisorbed oxygen corresponding to various reaction mechanisms as shown in Figure 6b. Both α -Fe₂O₃ {110} and {012} surfaces terminated with oxygen atoms cannot chemisorb O₂. Lattice oxygen in this case directly oxidizes CO thus creating oxygen vacancies in {110} and {012} surface layers.

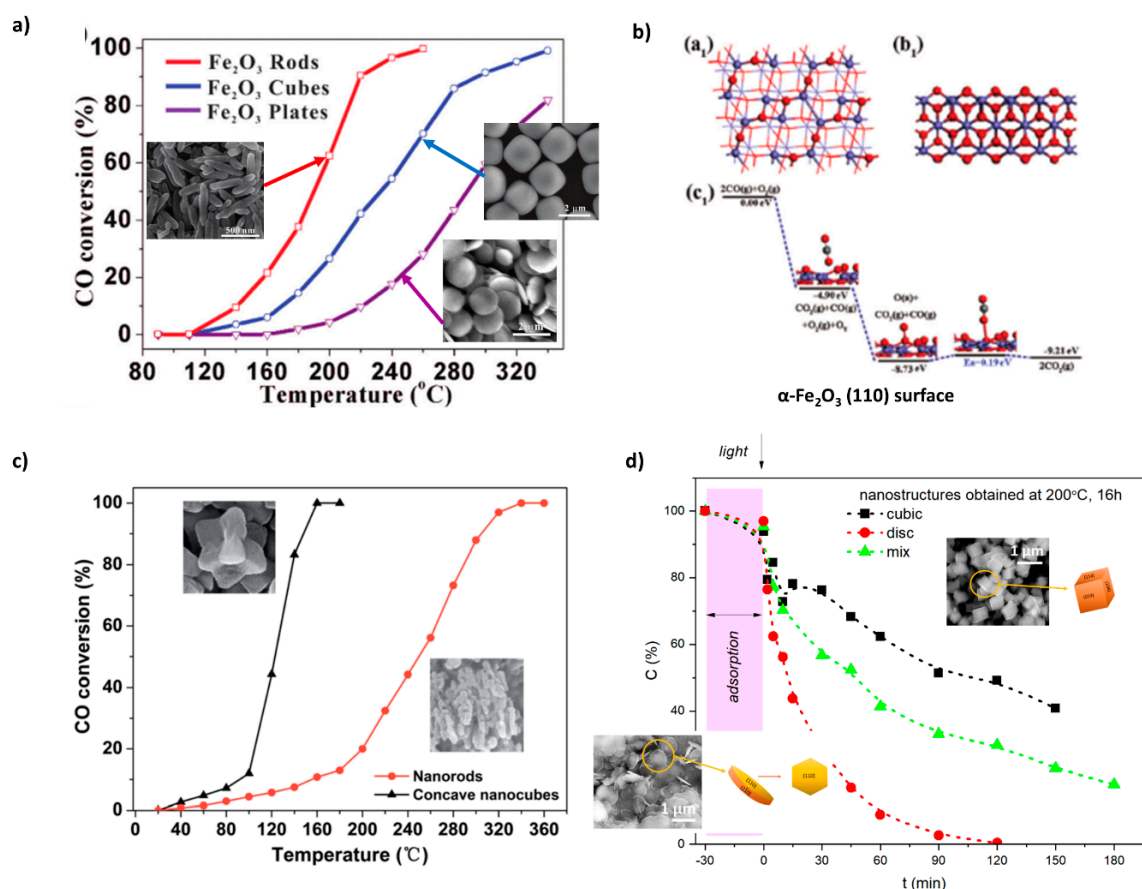


Figure 6. Catalytic activities of hematite: rods, cubes, plates (a) with the top and side view of optimized geometric structures of (110) surface with corresponding energy profiles of each elementary step in CO oxidation catalysis (b). Reprinted and modified with permission from ref. [175] Catalytic activities of concave nanocubes and nanorods α -Fe₂O₃ for carbon monoxide oxidation (c). Reprinted with permission from ref [124]. Photocatalytic degradation of RhB over the iron oxide various facet-dependent nanostructures (d). Reprinted and modified with permission from ref [126].

Then, O₂ chemisorbs at oxygen vacancy site and CO in the atmosphere reacts with this oxygen. Activation energy being lower for (110) surface—0.19 eV as compared with (012)—0.31 eV is a decisive factor in establishing the order mentioned above in the catalytic performance of microcrystals of different morphologies. Therefore, the activation energy in CO oxidation catalysis by α -Fe₂O₃ surfaces: 0.19 eV for (110) surface of rods < 0.31 eV for (012) surface of cubes < 0.39 eV for (001) surface of plates determines the order of the CO catalytic performance rods > cubes > plates.

Earlier, Liang et al. [124] gave evidence for the superior catalytic activity of hematite concave nanocubes for low-temperature oxidation (Figure 6c). Concave nanocubes were bound by high-index facets of much higher surface energy as compared with the case presented in [175]. Not only the conversion of CO was much more pronounced than in the case of cubes synthesized by Sun et al. [175], but the temperature onset was decreased to about 40 °C. No correlation with the specific surface area was found. Similar results were reported by Ouyang et al. [103] where pseudocubes of α -Fe₂O₃ enclosed within {012} facets displayed the best CO conversion ability as contrasted with bipyramid {113} and plate {001}/{012}. This effect has been explained by the different amounts of CO chemisorbed on these surfaces and related to the height of the barrier for activation of this process.

In order to investigate the photocatalytic activity of variously shaped crystals, dye photodegradation was performed [126]. Iron oxide nanostructures in the shape of nanodiscs and nanocubes were prepared by hydrothermal route with Zn²⁺ and Al³⁺ ions addition as capping agents. The influence of the well-defined facets towards photodegradation of rhodamine B under visible light irradiation with 5 mL of H₂O₂ as hydroxyl radicals source was investigated. It was shown (Figure 6d) that nanodiscs, with the dominant {110} facets exhibited the most desirable photocatalytic behavior, while the surface of cubic particles and powders with mixed morphology did not amplify the photodegradation processes. This significant improvement in photocatalytic activity in the presence of H₂O₂ was assigned to its diffusion at the {110} surface and easy generation of reactive species such as •OH.

4.3. Cu₂O

Cupric oxide Cu₂O contains Cu(I) that can either be reduced to Cu(0) or oxidized to Cu(II), thus it exhibits very rich chemical reactivity. Therefore, Cu₂O is well-known for its catalytic and photocatalytic applications [16,18,90,138,140,150]. The facet-dependent photodegradation of negatively charged methyl orange is the most widely studied for the photocatalytic activity investigation of Cu₂O crystals [96,97,155,179–182]. In some of these studies, particles with low-index and high-index facets have been examined [97,155,182] which indicated that high index facets displayed an enhanced catalytic activity.

It has been demonstrated [72] that Cu₂O {100} crystal planes are more stable than those of {111} and {110} during the oxidative dissolution reaction of Cu₂O. The stability order of Cu₂O {100}, {110}, and {111} crystal planes can be explained by the fact that the Cu–O bond on Cu₂O {100} surface is much shorter and stronger than that on Cu₂O {111} and {110} surfaces thus more difficult to break for the liquid–solid reactions to take place. Moreover, the Cu₂O {111} surface is easily reduced in contrast to the Cu₂O {100} surface. Cu₂O crystals have been extensively studied for numerous catalytic and photocatalytic reactions such as [3 + 2] cycloaddition [146], cross-coupling [183–185], water splitting [186] and CO oxidation [187].

Recently, the facet-dependent catalytic activity of Cu₂O nanocrystals of different shapes: cubes, octahedral, rhombic dodecahedra, but of the same total surface area, has been reported in the synthesis of 1,2,3-triazoles by multi-component, so-called “click” reactions of alkynes, organic halides, and NaN₃ [146]. “Click” chemistry is known for its powerful impact on drug discovery, organic synthesis, biological, and electrochemical applications [188,189]. The most practical aspect of click chemistry is the ability to attach diverse structures with a wide range of functional groups. The sequence of decreasing catalytic activity was detected: rhombic dodecahedral with exposed {110} facets, octahedral {111}, and nanocubes {100}.

Therefore, different types of exposed crystal planes {110}, {100} and {111} of Cu₂O nanocrystals exhibit different surface compositions/structures that determine their catalytic properties in catalytic reactions. As chemisorption plays a key role in the catalysis, the Cu(I) sites on Cu₂O surface exhibit a much stronger activity than the O sites, thus Cu₂O {100} surface terminated exclusively by the O sites is much less catalytically active than Cu₂O {110} and {111} surfaces [72].

Figure 7 gives examples of the application of shape-controlled nanocrystals of Cu₂O to dual-functional catalysis and clock reactions.

Dual-functional photocatalysis is an attractive process that seemed to be almost impossible to achieve in one system. However, it has been demonstrated [18] that Cu_2O cuboctahedrons allow to carry out photocatalytic pollutant degradation PDR and hydrogen evolution reactions HER in industrial wastewaters. It is difficult for PDR and HER to coexist in one system simultaneously as PDR is usually an anaerobic process whereas HER is an anoxic one [190]. Efficient charge carrier separation is necessary to achieve dual-functional photocatalysis and this could be done with electrons driving HER at {100} facets of Cu_2O and holes participating in PDR at {111} surfaces of Cu_2O , as shown in Figure 7d. Photoluminescence PL spectra presented in Figure 7a demonstrate that Cu_2O cuboctahedron with {100} and {111} facets exposed separately, the most efficiently, electrons and holes because the recombination rate, in this case, is the smallest. As an explanation of the mechanism of dual-functional catalysis, it was proposed to take into account the work function of different facets and compare them with that of bulk Cu_2O (4.8 eV). It turned out that the work function of Cu_2O (100) facet (7.8 eV) was larger than that of the bulk Cu_2O while that of Cu_2O {111} was exactly the same (4.8 eV) [191]. Therefore, electrons accumulate preferentially on the {100} facet whereas holes rest on the {111} surface of the nanocrystal. The presence of a hole in the dye degradation was established by using different quenchers in vacuum (Figure 7b) and in the atmosphere (Figure 7c). Photocatalytic activity was greatly inhibited by ethylene diamine tetraacetic acid EDTA—a quencher of holes, which proved that h^+ were the main species active in PDR.

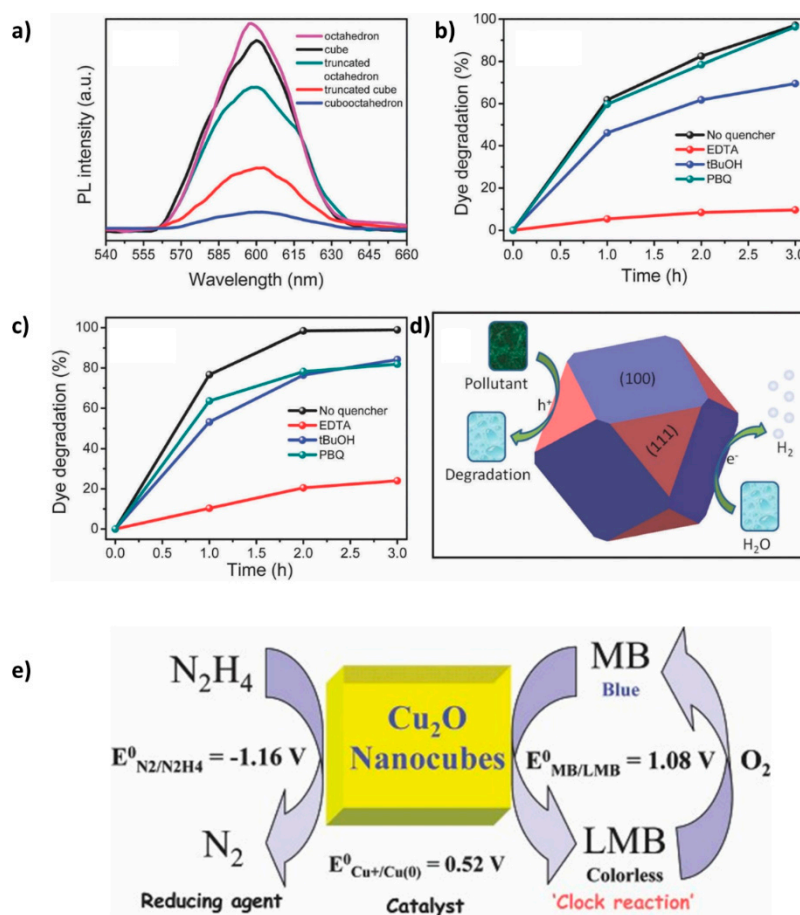


Figure 7. PL spectra of Cu_2O facet dependent nanocrystal (a) with corresponding photocatalytic degradation of RhB over the cuboctahedrons in the presence of radical quenchers in vacuum (b), in the atmosphere (c), and schematic illustration of their dual-functional photocatalytic mechanism (d). Reprinted with permission from ref. [18] Mechanism of 'clock reaction' of Cu_2O nanocubes (e). Reprinted with permission from ref. [140].

The most spectacular manifestation of the catalysis performed with the aid of Cu₂O nanoparticles is the “clock reaction” involving methylene blue MB and hydrazine in aqueous medium [140]. A clock reaction is a chemical reaction which gives rise to a significant induction period during which one of the chemical species, the clock chemical, has a very low concentration. The end of the induction period is marked by a rapid increase in the concentration of the clock chemical. Demonstration of the clock reactions is quite popular in chemistry and may be carried out with different substrates, e.g., sulfuric acid and hydrogen peroxide with iodine. As shown in Figure 7e, hydrazine supplies electrons to MB via nanocube of Cu₂O which acts for many days as a catalyst in a solution. Colorless leucomethylene blue, LMB is produced as a consequence but the blue color of MB can be regenerated in a few seconds after being shaken in air which promotes oxidation. Importance of Cu₂O nanoparticles in this clock reactions has been established beyond doubt as the electron transfer from hydrazine to MB required the presence of the catalysts and was made possible because of the reasonable affinity of the reducing hydrazine and oxidant MB to the nanocube surfaces as shown in Figure 7e.

5. Chemical Sensing

Chemical sensing especially at close to room temperature is considered as dominated by surface processes. Two factors determine the reactivity of a solid in the gas-solid chemical reactions: the surface reactivity of the solid and the adsorption/activation of gas molecules on the solid surface. These two factors have to be optimized in order to achieve improved sensor response but at the same time selectivity to target gas can be increased by a careful choice of active surfaces of micro and nanocrystals.

In the case of gas sensing, chemisorption of oxygen in different forms O₂[−], O[−] and O^{2−} takes place as the first step in air atmosphere at the temperature below 150 °C, between 150 °C and 400 °C, and above 400 °C, respectively [31]. Reaction (1) describes generally this process and indicates that the electrons from the bulk of the solid have to be involved in chemisorption of oxygen species. As a result, a depletion in the case of n-type or accumulation layer in the case of p-type is formed at the interface solid-gas thus creating a potential barrier for the current flow. Depletion layer width may depend on the facet exposed in the case of micro and nanocrystals as shown schematically in Figure 8 for an n-type semiconductor. In the second step, when the same facet is exposed to reducing gas, e.g., CO, the electrons are exchanged and the barrier height decreases. Exposure of high-energy facets with a considerable density of the dangling bonds is believed to improve adsorption of gas molecules thus affecting gas sensing responses.

When discussing the mechanism of gas sensing by metal oxide semiconductors, it is important to consider the relationship between the grain size, d , and Debye length, λ_D , defined as:

$$\lambda_D = \sqrt{\frac{\epsilon\epsilon_0\phi_s}{eN_D}} \quad (7)$$

where ϵ and ϵ_0 denote relative permittivity of the material and vacuum permittivity, respectively, ϕ_s is the surface potential barrier, e represents electron charge and N_D stands for donor concentration.

Debye length determines the width of the near-surface depletion or accumulation layer, thus when compared with the grain size, one can distinguish between three different cases, namely:

- large grains: $d \gg \lambda_D$
- intermediate case: $d \geq \lambda_D$
- small grains: $d \leq \lambda_D$

For large grains, the depletion or accumulation layer constitutes an insignificant part of the grain and the interaction between gas phase and sensing material can be analyzed in the same way as for the bulk material. Most of the volume of the crystallites is unaffected by the surface interactions with the gas phase.

The gas sensing mechanism is controlled by the grain boundaries barriers and charge transfer from one grain to another. The electrical conductivity σ depends exponentially on the barrier height:

$$\sigma \propto \exp\left(\frac{-qV_B}{kT}\right) \quad (8)$$

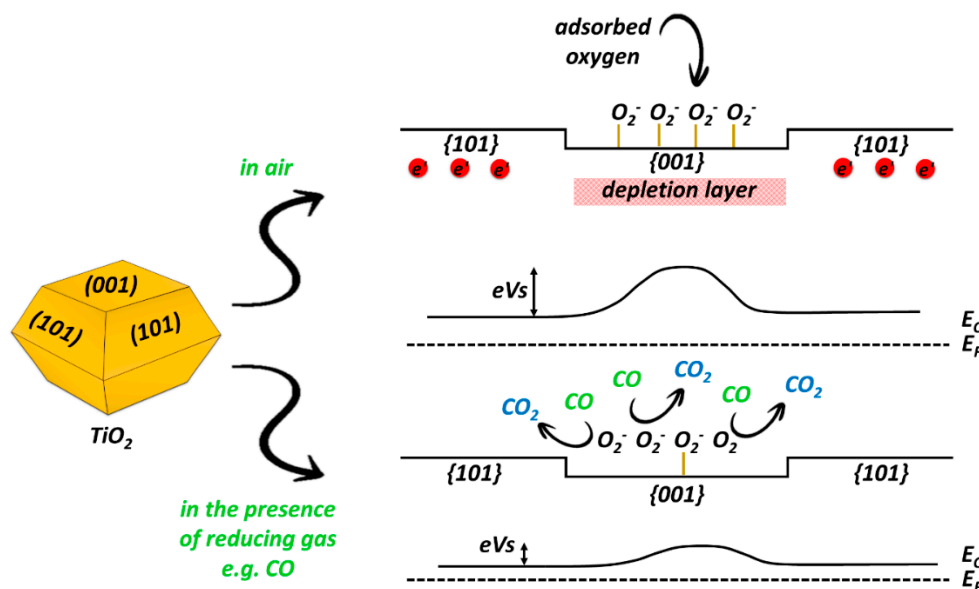


Figure 8. Schematic illustration of facet-dependent sensing mechanism for n-type semiconductor in the presence of air and reducing gas e.g., CO.

Furthermore, the grain boundaries barriers are independent of the grain size, therefore, the sensitivity is independent of the average crystallite size.

If the grain size is reduced then a significant part of the volume participates in the interaction. The energy bands are nearly flat throughout the whole structure and, since there are no significant barriers for intercrystallite charge transport, the conductivity is controlled by the intercrystallite conductivity.

As far as nanomaterials are concerned, the surface-to-volume ratio, A/V , is thought to be one of the most important parameters to improve gas sensing characteristics, since it is inversely proportional to the particle size. Under the assumption of identical, spherical particles of the radius r and diameter $D = 2r$ one can use the following simplified equation:

$$\frac{A}{V} = \frac{4\pi r^2}{\frac{4}{3}\pi r^3} = \frac{6}{D} \quad (9)$$

The surface-to-volume ratio affects, among others, the density of centers active for chemisorption [77,129,192,193] thus facilitates the interactions between the solid surface and gas phase.

However, it has been recently recognized [33,102,194–196] that high surface-to-volume ratio cannot guarantee excellent gas sensing performance. There are certainly other factors related to surface properties such as surface atomic arrangement, surface energy, dangling bond density, etc. that cannot be made explicit in the case of randomly oriented nanomaterials but that can be elucidated and exploited in the case of shape-controlled nanocrystals. Thus, recently substantial research has been initiated to take advantage of the selective exposure of high-energy facets of numerous metal oxide nanocrystals such as SnO₂ [197–200], ZnO [198,201–205], WO₃ [198,206], anatase TiO₂ [9,106,112], α -Fe₂O₃ [129,132,134,135], Cu₂O [27,76,78,139,144,148] and their anisotropic properties to improve gas sensing behavior. The chosen examples that follow, illustrate this new trend.

5.1. TiO₂ (Anatase)

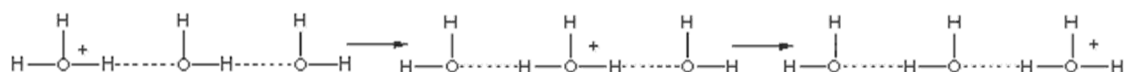
Titanium dioxide is a promising material for a sensor capable of detecting a variety of reducing gases, i.e., NH₃ [207], CO [208], H₂ [209], H₂S [210] and alcohols [211].

Anatase TiO₂ is known as a good candidate for gas sensors based on the surface reactions. Applications of anatase in gas sensing [212–214] are inherently related to the progress in synthesis of nanomaterials that, due to a substantial increase in surface-to-volume ratio, enable low-temperature operation. Not only nanotubes [215] but other, sometimes even exotic nanoforms have been tested as gas sensors [214]. Our own work in this field [216] indicates that a synergetic effect in H₂ sensing is produced when rutile and anatase nanopowders are mixed in a certain proportion.

It is generally believed that due to high surface energy, TiO₂ anatase nanocrystals with the exposed {001} facets should display the best gas sensing behavior [8–10]. Figure 9 recapitulates the most important results concerning the influence of shape-controlled TiO₂ nanocrystals grown by hydrothermal method on their response to ethanol.

Quite recently Liu et al. [9,10] reported that TiO₂ nanosheets with exposed {001} high energy facets demonstrated abnormal p-type sensing response to 500 ppm of ethanol below 120 °C, followed by switching to a regular n-type behavior above (250 °C) as shown in Figure 9a.

The ethanol-sensing performance of the sensors constructed on the basis of TiO₂ nanocrystals with various percentage of the exposed {001} facets was also investigated by Liu [9] as shown in Figure 9c–f. There is a strong correlation between the crystallite size and the shape controlled by HF volume during the crystal growth (Figure 9b). It is quite evident that with the increasing percentage of the exposed {001} facets, the response increases in both cases: p and n-type regime. Abnormal p-type sensing behavior was accounted for by proton transfer between alcohol molecules and water molecules adsorbed at lower temperatures at the surface of TiO₂ nanosheets. At high coverage of the hydrophilic TiO₂ surface by water molecules, the proton conduction is facilitated. According to the Grotthuss chain mechanism [217,218], proton conduction takes place according to the Scheme 1 as shown below:



Scheme 1. Reactions of hydrated hydronium ions and hydrated hydroxide ions. Reprinted with permission from ref. [219]

After the introduction of ethanol, its molecules can be dissolved in the pre-adsorbed water. Due to the larger proton affinity of ethanol (188.3 kcal/mol) as compared to that of H₂O (166.5 kcal/mol), protons will be bonded by ethanol molecules [218] leading to the formation of a great quantity of C₂H₅OH₂⁺·(H₂O)₂ ions. This results in a substantial resistance increase of the water layer on the surface of TiO₂, responsible for the abnormal p-type sensing response. With humidity increase, more C₂H₅OH₂⁺·(H₂O)₂ ions are generated, and electrical resistance is thus increased. When the operation temperature is higher than 150 °C, water molecules desorb from the surface of TiO₂ nanosheets. In this case, oxygen adsorption replaces the water adsorption, and a regular n-type sensing response is exhibited at elevated temperatures above 250 °C.

Huang et al. [106] studied the gas responses of TiO₂-based nanosensors of different shapes: nanorods, nanobelts, nano-polyhedrons, and nanoparticles under a certain concentration of ethanol at the temperature of 400 °C. It is apparent that different morphologies of TiO₂ result in different gas-sensing properties affecting not only the response but its kinetics as well. The response and recovery times were found to be 9 and 7 s, respectively for the nanoparticles, 6 and 5 s, respectively for the nanobelts, 6 and 4 s, respectively for the nanorods, and 5 and 4 s, respectively for nano-polyhedrons, and the gas sensing responses of nanoparticles, nanobelts, nano-polyhedrons, nanorods were estimated to be 8.4, 9.6, 18.8, and 13.3, respectively.

Zhang [112] performed the first-principle studies as well as experimental verification of enhanced CO sensing by TiO₂ with exposed {001} facet. Surface orientation was found to have great influence on CO adsorption, the mechanism of which was clarified by the DFT simulation, where (001) surface displayed stronger interaction with CO.

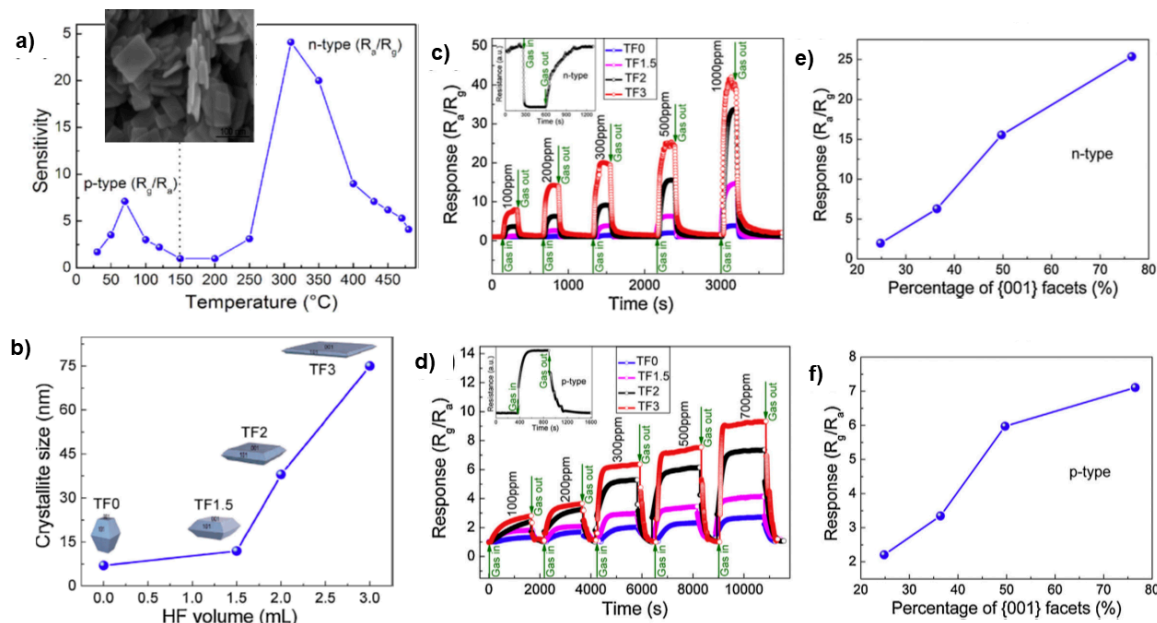


Figure 9. The sensitivity of TiO₂ nanosheet-based sensor to 500 ppm alcohol at various temperatures and a typical SEM image (a). The average crystallite size and the corresponding schematic shape of TiO₂ nanocrystals as a function of the HF amount (b), the response with recovery curves of the sensors based on the four kinds of TiO₂ samples as a function of ethanol concentration at the operating temperatures of 310 °C (c) and 70 °C (d). Response values of the sensors based on the four kinds of TiO₂ samples (up to 500 ppm of ethanol) as a function of the percentage of exposed {001} facets at 310 °C (e) and at 70 °C (f). Reprinted with permission from ref. [9,10].

5.2. α -Fe₂O₃ (Hematite)

Recently published an excellent review on gas sensing properties of α -Fe₂O₃ based nanomaterials by Mirzaei et al. [11] suggests that hematite is the sixth most studied metal oxide for this application.

Hematite α -Fe₂O₃ is generally more sensitive to alcohols and NO₂. A lot of papers appeared on different forms of nanostructured α -Fe₂O₃ [220–222] for gas sensing. Adsorption of water acting as a donor has an important influence on its electronic properties [11].

However, there are not so many reports on the application of shape-controlled α -Fe₂O₃ nanocrystals. The representative results are shown in Figure 10.

Liu et al. [132] studied rhomboidal crystals of α -Fe₂O₃ with exposed {104} facets for acetone (Figure 10a) and ethanol (Figure 10b,) and compared their responses with those of α -Fe₂O₃ commercial powder. For a given acetone and ethanol concentration, the sensor response of well-oriented crystals is significantly higher than that of the chaotically dispersed powder grains. This result may be attributed to the specific arrangement of Fe atoms on the (104) plane. Unsaturated coordination form of Fe atoms has been proposed in this case. Therefore, a large concentration of dangling bonds or oxygen vacancies appear on {104} plane making this surface highly reactive towards adsorption of oxygen species in the first stage of gas sensing.

Yang et al. [34] reported the synthesis of polyhedral single-crystalline α -Fe₂O₃ particles by the hydrothermal method and applied them to sensing of the following chemical compounds: acetic acid, ammonia, methanol, acetone, methanal, and ethanol, as shown in Figure 10c. Two different shapes were discussed: oblique parallelepiped and tetrakaidecahedron. The sensitivity to ethanol over all

concentration range studied follows the sequence: oblique parallelepiped > less truncated degree polyhedron > more truncated degree polyhedron > quasi-spherical structure as can be concluded from Figure 10d. This effect has been attributed to high-index planes enclosing the oblique parallelepiped.

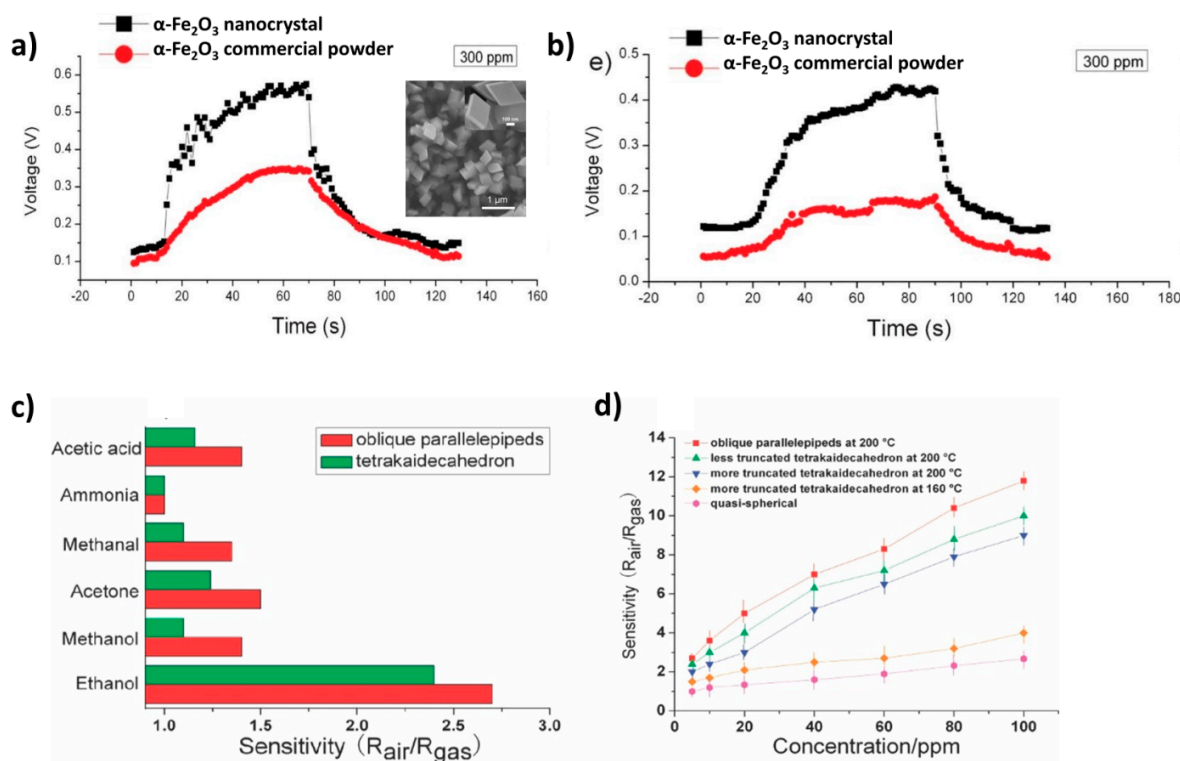


Figure 10. Dynamic response–recovery curves for acetone (a) and ethanol (b) detection (300 ppm). Reprinted and modified with permission from ref. [134]. Sensitivity of the sensors based on as-prepared hematite towards different gases or vapors at a concentration of 5 ppm (c). Sensitivity curves of hematite particles with different shapes as a function of ethanol concentration (d). Reprinted and modified with permission from ref. [34].

Similar observations were made by Ouyang [129] and Liu [135]. Ouyang et al. [129] demonstrated that the bipyramid Fe₂O₃-{113} nanocrystals exhibited the best performance in acetone detection, followed by pseudo cube-Fe₂O₃-{012} and plate-Fe₂O₃-{001}/{012}. The same facet-dependent sensing order was found in the methanol sensing measurements. It was therefore concluded that the gas sensing properties of bare crystal surfaces were in the order of {113} > {012} > {001}. For three different samples, the relative percentages of the chemisorbed oxygen component are about 56.85% (bipyramid-Fe₂O₃-{113}), 35.40% (pseudo cube-Fe₂O₃-{012}), and 22.92% (plate-Fe₂O₃-{001}/{012}), respectively. Therefore the {113} facets of α -Fe₂O₃ are more active than the {012} and {001} facets for adsorption of ionized oxygen species.

5.3. Cu₂O

Cu₂O is an excellent example of a p-type semiconductor of gas sensing mechanism different than that of materials exhibiting an n-type conductivity (TiO₂, Fe₂O₃). The basic difference in gas sensing mechanism comes from the fact that instead of the depletion region, an accumulation layer enriched in holes is formed at the surface upon interaction with atmospheric oxygen [223,224]. As a consequence, the electrical resistance of this layer decreases with respect to the bulk. It means that the conduction in the sensing layer will take place differently than in the case of n-type metal oxides. The electrical current in the space charge layer flows “parallel” to the surface, not perpendicular as in the case of n-type sensors, and through the bulk. Therefore, the space charge layer resistance, which is sensitive to

gas chemisorption, is not dominating the overall resistance like in the case of n-type sensors. According to the model proposed by Barsan et al. [223] the resulting gas sensor response for p-type semiconductor (Equation (10)), S_p is expected to be much smaller than that of n-type metal oxide, S_n and in the case of the same morphology one gets:

$$S_p = \sqrt{S_n} \quad (10)$$

Therefore, the number of papers devoted to p-type metal oxides in application to gas sensing is much smaller as compared with that of n-type semiconductors. However, there is still a great challenge to develop sensitive and selective gas sensors based on p-type semiconductors such as CuO [225] and Cu₂O [226–229].

Cuprous oxide materials enclosed with well-defined facets have been widely investigated in the field of electrochemical sensing, especially in hydrogen peroxide, H₂O₂, or glucose detection [139,144]. H₂O₂ is a common oxidizing agent and essential intermediate in medicine, industry or electrochemistry [230,231]. Due to the low cost, simple operation and high sensitivity nonenzymatic electrode-based electrochemical methods hold a great promise.

Zhong et al. [144] analyzed different electrodes modified by variously shaped Cu₂O nanocrystals for H₂O₂ detection (Figure 11a,b). Responses indicated that the presence of dangling bonds at the {111} and {110} surfaces, which are positively charged, plays a significant role in the adsorption processes. The {100} facets do not interact with hydroxyl radicals in the solution due to their electrically neutral behavior. The extended hexapod Cu₂O with a high contribution from {111} facets exhibits the best electrocatalytic activity toward H₂O₂. The following order in the H₂O₂ detection has been established: extended hexapod > octahedral > rhombic dodecahedra which correlates well with the electrocatalytic activity.

On the other hand, similar relationship was studied by Wang et al. [33], who analyzed CO response of cuprous oxide in a form of a cube, octa- and truncated octahedral crystals (Figure 11c). It was suggested that Cu₂O-octa and Cu₂O-truncated octahedra exhibited the conductivity higher than that of cube Cu₂O due to the presence of surfaces with different degrees of band bending. The reaction rate between target gas molecules and the surface of sensing oxide was enhanced. Moreover, according to the model for {100} facets terminated by oxygen atoms only, while copper atoms are coordinate saturated, the electrically neutral {100} facets are catalytically inactive. The probability of interactions with ionized oxygen species is negligible in contrast to {111} facet, where copper atoms are coordinated unsaturated. Therefore, an increase in the number of ionized oxygen species adsorbed onto the {111} facets can be observed which significantly affects the sensing activity of the Cu₂O-octa crystals.

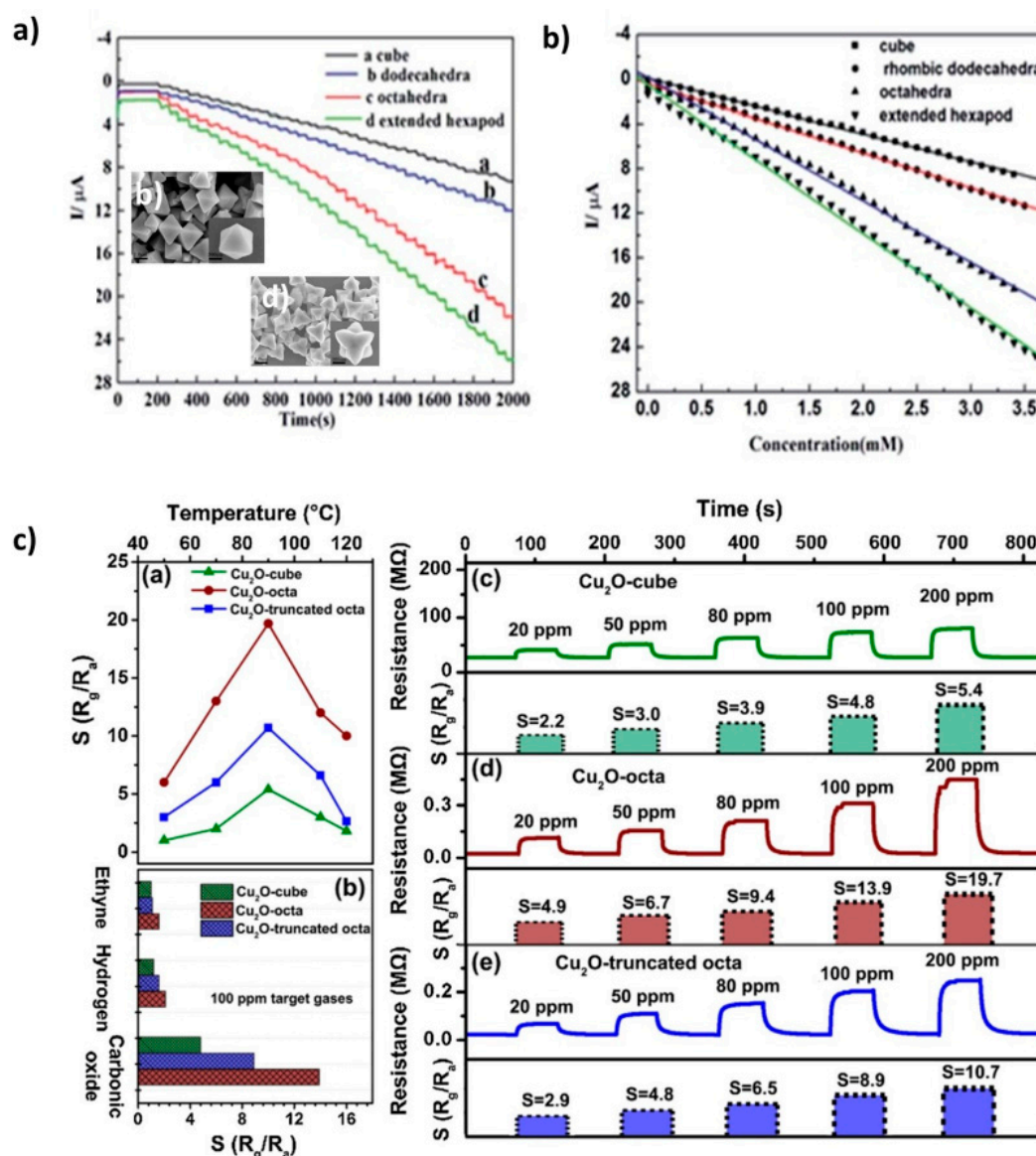


Figure 11. Amperometric response of four different Cu₂O modified electrodes (a) with the corresponding calibration curves of oxidation currents versus H₂O₂ concentrations (b). Reprinted and modified with permission from ref. [146]. The relationship of working temperature and sensing response of various shaped Cu₂O towards CO, H₂, and C₂H₂ with dynamic curves and gas response values (c). Reprinted with permission from ref. [33].

6. Conclusions and Perspectives.

This review was intended to present the relatively new approach in the design of photocatalytic and gas sensing materials, i.e., shape-controlled nanocrystals with well-defined facets exposed. Research performed in this field, directed at the growth and morphology, as well as photocatalytic and chemical sensing applications of particular metal oxides such as TiO₂—anatase, α -Fe₂O₃ hematite, and Cu₂O has been cited and discussed. Other metal oxides such as SnO₂, ZnO, WO₃, Bi₂O₃, BiVO₄, also deserve special attention and should be carefully reviewed in this aspect in the future.

Common to both applications is a fact that for a reaction to take place, molecules need to adsorb on the nanocrystal surfaces. Surface energy, surface charge, the number of active catalytic and sensing sites, as well as binding energy of molecules to a particular surface are relevant factors to consider in evaluating the relative catalytic activities and sensitivities of different crystal faces to particular target species. Moreover, for photodegradation and photo-catalyzed reactions, the efficient

transport of photogenerated charge carriers to the particle surfaces is important while selectivity plays a fundamental role in the case of chemical sensors.

Single crystals exhibit the capability of selectively exposing crystal facets on the surface, thereby fulfilling the requirement of anisotropy in electrical, optical, and catalytic properties. However, special methods of growth of highly desired facets, i.e., those of the highest surface energy and sufficient density of dangling bond are needed as according to laws of thermodynamics, the low energy facets usually terminate nanocrystals with equilibrium shape. One of the strategies which can be pursued in order to effectively reverse this situation, i.e., to stabilize the more reactive facets, is the selection of the optimal working conditions. Preparation of nanocrystals enclosed within particular facets is not enough from the point of view of identification of factors efficiently controlling the particle shape as well as the mechanism of growth. As already pointed out in this review, it is more challenging to synthesize nanocrystals with a series of shapes by changing only one technological parameter. Moreover, it is desirable to avoid application of hydrofluoric acid and other highly toxic compounds in order to promote the “green chemistry” scenario.

Although some impressive improvement has been observed with respect to catalysis and photocatalysis based on TiO₂ shape-controlled nanocrystals, there is still a lot to be done in the case of other metal oxides: α -Fe₂O₃ and Cu₂O. Systematic studies of the effect of high-index planes on the photocatalytic decomposition of contaminants are required to form more general conclusions as to the order of facets responsible for the photocatalytic activity. It has been established without any doubt that selectivity of the photocatalytic processes is provided by the charge transfer to different facets where particular molecules can be adsorbed. No such mechanism has been suggested in the case of chemical sensing. In conclusion, increasing the percentage of high activity facets helps to develop highly efficient photocatalysts. Nevertheless, a synergism of different facets on the surface of semiconducting crystals is also exploited.

Many serious challenges still remain in the area of chemical sensing especially as far as gas sensitive nanocrystals are considered. The gas sensing mechanism being different for n-type and p-type semiconductors and the lack of selectivity in the case of resistive-type metal oxide gas sensors complicates the task of application of shape-controlled nanocrystals for this purpose.

However, important advancements in this field, allow us to expect future development of sensitive and selective gas sensors based on facet-engineered nanocrystals with the well-understood surface chemistry. Such progress in both research areas: catalysis and chemical sensing, will certainly bring us closer to the realization of efficient, tailor-made and tunable nanomaterials.

Author Contributions: All the authors contributed equally to the preparation the manuscript: A.K. was mainly responsible for resources and editing, M.S. visualization and editing, K.Z. original draft preparation, M.R. conceptualization and supervision.

Funding: This work was financed by the National Science Centre, Poland (NCN). MR acknowledges project number UMO-2016/21/B/ST8/00457, KZ acknowledges project number UMO-2016/23/B/ST7/00894, AK acknowledges project number UMO-2016/23/D/ST8/00024

Conflicts of Interest: The authors declare no conflict of interest.

References

1. Yu, J.; Dai, G.; Xiang, Q.; Jaroniec, M. Fabrication and enhanced visible-light photocatalytic activity of carbon self-doped TiO₂ sheets with exposed {001} facets. *J. Mater. Chem.* **2011**, *21*, 1049–1057. [[CrossRef](#)]
2. Pal, J.; Pal, T. Faceted metal and metal oxide nanoparticles: Design, fabrication and catalysis. *Nanoscale* **2015**, *7*, 14159–14190. [[CrossRef](#)] [[PubMed](#)]
3. Huang, M.H.; Lin, P.H. Shape-controlled synthesis of polyhedral nanocrystals and their facet-dependent properties. *Adv. Funct. Mater.* **2012**, *22*, 14–24. [[CrossRef](#)]
4. Huang, M.H.; Rej, S.; Hsu, S.C. Facet-dependent properties of polyhedral nanocrystals. *Chem. Commun.* **2014**, *50*, 1634–1644. [[CrossRef](#)] [[PubMed](#)]

5. Bai, S.; Wang, L.; Li, Z.; Xiong, Y. Facet-engineered surface and interface design of photocatalytic materials. *Adv. Sci.* **2017**, *4*. [[CrossRef](#)] [[PubMed](#)]
6. Wang, H.; Qiao, L.; Xu, H.; Lin, Y.; Shen, Y.; Nan, C. Anisotropy of photocatalytic properties in nanostructured photocatalysts. *Soft Nanosci. Lett.* **2016**, *6*, 11–30. [[CrossRef](#)]
7. Kang, D.; Kim, T.W.; Kubota, S.R.; Cardiel, A.C.; Cha, H.G.; Choi, K.S. Electrochemical synthesis of photoelectrodes and catalysts for use in solar water splitting. *Chem. Rev.* **2015**, *115*, 12839–12887. [[CrossRef](#)] [[PubMed](#)]
8. Gao, X.; Zhang, T. An overview: Facet-dependent metal oxide semiconductor gas sensors. *Sens. Actuators B Chem.* **2018**, *277*, 604–633. [[CrossRef](#)]
9. Liu, C.; Lu, H.; Zhang, J.; Gao, J.; Zhu, G.; Yang, Z.; Yin, F.; Wang, C. Crystal facet-dependent p-type and n-type sensing responses of TiO₂ nanocrystals. *Sens. Actuators B Chem.* **2018**, *263*, 557–567. [[CrossRef](#)]
10. Liu, C.; Lu, H.; Zhang, J.; Yang, Z.; Zhu, G.; Yin, F.; Gao, J.; Chen, C.; Xin, X. Abnormal p-type sensing response of TiO₂ nanosheets with exposed {001} facets. *J. Alloys Compd.* **2017**, *705*, 112–117. [[CrossRef](#)]
11. Mirzaei, A.; Hashemi, B.; Janghorban, K. α -Fe₂O₃ based nanomaterials as gas sensors. *J. Mater. Sci. Mater. Electron.* **2016**, *27*, 3109–3144. [[CrossRef](#)]
12. Zeng, W.; Liu, T.; Gou, Z.; Lin, L. Carbon monoxide sensing mechanism of highly oriented TiO₂ from first principles. *Phys. E Low-Dimens. Syst. Nanostruct.* **2012**, *44*, 1567–1571. [[CrossRef](#)]
13. Li, T.; He, M.; Zeng, W. Polyhedral Cu₂O crystal: Morphology evolution from meshed nanocube to solid and gas-sensing performance. *J. Alloys Compd.* **2017**, *712*, 50–58. [[CrossRef](#)]
14. Xie, Z.; Han, N.; Li, W.; Deng, Y.; Gong, S.; Wang, Y.; Wu, X.; Li, Y.; Chen, Y. Facet-dependent gas sensing properties of Cu₂O crystals. *Phys. Status Solidi Appl. Mater. Sci.* **2017**, *214*. [[CrossRef](#)]
15. Liu, C.; Han, X.; Xie, S.; Kuang, Q.; Wang, X.; Jin, M.; Xie, Z.; Zheng, L. Enhancing the photocatalytic activity of anatase TiO₂ by improving the specific facet-induced spontaneous separation of photogenerated electrons and holes. *Chem. Asian J.* **2013**, *8*, 282–289. [[CrossRef](#)]
16. Zhang, Y.H.; Jiu, B.B.; Gong, F.L.; Chen, J.L.; Zhang, H.L. Morphology-controllable Cu₂O supercrystals: Facile synthesis, facet etching mechanism and comparative photocatalytic H₂ production. *J. Alloys Compd.* **2017**, *729*, 563–570. [[CrossRef](#)]
17. Kuang, Q.; Wang, X.; Jiang, Z.; Xie, Z.; Zheng, L. High-energy-surface engineered metal oxide micro- and nanocrystallites and their applications. *Acc. Chem. Res.* **2014**, *47*, 308–318. [[CrossRef](#)]
18. Lin, Z.; Li, L.; Yu, L.; Li, W.; Yang, G. Dual-functional photocatalysis for hydrogen evolution from industrial wastewaters. *Phys. Chem. Chem. Phys.* **2017**, *19*, 8356–8362. [[CrossRef](#)]
19. Zhou, K.; Wang, X.; Sun, X.; Peng, Q.; Li, Y. Enhanced catalytic activity of ceria nanorods from well-defined reactive crystal planes. *J. Catal.* **2005**, *229*, 206–212. [[CrossRef](#)]
20. Paulose, M.; Varghese, O.K.; Mor, G.K.; Grimes, C.A.; Ong, K.G. Unprecedented ultra-high hydrogen gas sensitivity in undoped titania nanotubes. *Nanotechnology* **2006**, *17*, 398–402. [[CrossRef](#)]
21. Yoshida, R.; Suzuki, Y.; Yoshikawa, S. Syntheses of TiO₂ (B) nanowires and TiO₂ anatase nanowires by hydrothermal and post-heat treatments. *J. Solid State Chem.* **2005**, *178*, 2179–2185. [[CrossRef](#)]
22. Suber, L.; Imperatori, P.; Ausanio, G.; Fabbri, F.; Hofmeister, H.; Stazione, M.; Fische, I.S. Synthesis, morphology, and magnetic characterization of iron oxide nanowires and nanotubes. *J. Phys. Chem. B* **2005**, *109*, 7103–7109. [[CrossRef](#)]
23. Fan, Z.; Wen, X.; Yang, S.; Lu, J.G. Controlled p- and n-type doping of Fe₂O₃ nanobelt field effect transistors. *Appl. Phys. Lett.* **2005**, *87*, 8–11. [[CrossRef](#)]
24. Qiao, L.; Swihart, M.T. Solution-phase synthesis of transition metal oxide nanocrystals: Morphologies, formulae, and mechanisms. *Adv. Colloid Interface Sci.* **2017**, *244*, 199–266. [[CrossRef](#)]
25. Yang, H.G.; Sun, C.H.; Qiao, S.Z.; Zou, J.; Liu, G.; Smith, S.C.; Cheng, H.M.; Lu, G.Q. Anatase TiO₂ single crystals with a large percentage of reactive facets. *Nature* **2008**, *453*, 638–641. [[CrossRef](#)]
26. Cuenya, B.R.; Beharfarid, F. Nanocatalysis: Size- and shape-dependent chemisorption and catalytic reactivity. *Surf. Sci. Rep.* **2015**, *70*, 135–187. [[CrossRef](#)]
27. Shang, Y.; Guo, L. Facet-Controlled Synthetic Strategy of Cu₂O-Based Crystals for Catalysis and Sensing. *Adv. Sci.* **2015**, *2*, 1500140(1)–1500140(22). [[CrossRef](#)]
28. Liu, L.; Jiang, Y.; Zhao, H.; Chen, J.; Cheng, J.; Yang, K.; Li, Y. Engineering coexposed {001} and {101} facets in oxygen-deficient TiO₂ nanocrystals for enhanced CO₂ photoreduction under visible light. *ACS Catal.* **2016**, *6*, 1097–1108. [[CrossRef](#)]

29. Wulff, G. Zur Frage der Geschwindigkeit des Wachstums und der Auflösung der Krystallflächen. In *Zeitschrift für Kristallographie—Crystalline Materials*; Pöttgen, R., Ed.; Oldenbourg Wissenschaftsverlag GmbH: Berlin, Germany, 1895; pp. 449–530. ISSN 2196-7105.
30. Lazzeri, M.; Vittadini, A.; Selloni, A. Structure and energetics of stoichiometric TiO₂ anatase surfaces. *Phys. Rev. B Condens. Matter Mater. Phys.* **2001**, *63*, 1554091–1554099. [\[CrossRef\]](#)
31. Barsan, N.; Weimar, U.D.O. Conduction model of metal oxide gas sensors. *J. Electroceram.* **2002**, *7*, 143–167. [\[CrossRef\]](#)
32. Wang, Y.L.; Li, Y.H.; Wang, X.L.; Hou, Y.; Chen, A.P.; Yang, H.G. Effects of redox mediators on α -Fe₂O₃ exposed by {012} and {104} facets for photocatalytic water oxidation. *Appl. Catal. B Environ.* **2017**, *206*, 216–220. [\[CrossRef\]](#)
33. Wang, L.; Zhang, R.; Zhou, T.; Lou, Z.; Deng, J.; Zhang, T. P-type octahedral Cu₂O particles with exposed {111} facets and superior CO sensing properties. *Sens. Actuators B Chem.* **2017**, *239*, 211–217. [\[CrossRef\]](#)
34. Yang, Y.; Ma, H.; Zhuang, J.; Wang, X. Morphology-controlled synthesis of hematite nanocrystals and their facet effects on gas-sensing properties. *Inorg. Chem.* **2011**, *50*, 10143–10151. [\[CrossRef\]](#)
35. Hellwege, K.H.; Hellwege, A.M.; Landolt, H.; Börnstein, R.; Madelung, O.; Callomon, J.H. *Landolt-Bornstein: Numerical data and functional relationships in Science and Technology—new series*; Springer: New York, NY, USA, 2015; Volume 1.
36. Mo, S.-D.; Ching, W.Y. Electronic and optical properties of three phases of titanium dioxide: Rutile, anatase, and brookite. *Phys. Rev. B* **2000**, *51*, 13023–13032. [\[CrossRef\]](#)
37. Seo, M.H.; Yuasa, M.; Kida, T.; Huh, J.S.; Shimano, K.; Yamazoe, N. Gas sensing characteristics and porosity control of nanostructured films composed of TiO₂ nanotubes. *Sens. Actuators B Chem.* **2009**, *137*, 513–520. [\[CrossRef\]](#)
38. Tang, J.; Zhang, X.; Xiao, S.; Zeng, F. Application of TiO₂ nanotubes gas sensors in online monitoring of SF₆ insulated equipment. *Intech Open* **2015**, *2*, 75–122. [\[CrossRef\]](#)
39. Park, J.A.; Moon, J.; Lee, S.J.; Kim, S.H.; Zyung, T.; Chu, H.Y. Structure and CO gas sensing properties of electrospun TiO₂ nanofibers. *Mater. Lett.* **2010**, *64*, 255–257. [\[CrossRef\]](#)
40. Radecka, M.; Jasinski, M.; Klich-Kafel, J.; Rekas, M.; Lyson, B.; Czapla, A.; Lubecka, M.; Sokolowski, M.; Zakrzewska, K.; Heel, A.; et al. TiO₂-based nanopowders for gas sensor. *Ceram. Mater.* **2010**, 545–549.
41. Lyson-Sypien, B.; Czapla, A.; Lubecka, M.; Kusior, E.; Zakrzewska, K.; Radecka, M.; Kusior, A.; Balogh, A.G.; Lauterbach, S.; Kleebe, H.J. Gas sensing properties of TiO₂-SnO₂ nanomaterials. *Sens. Actuators B Chem.* **2013**, *187*, 445–454. [\[CrossRef\]](#)
42. Li, J.; Yu, Y.; Chen, Q.; Li, J.; Xu, D. Controllable synthesis of TiO₂ single crystals with tunable shapes using ammonium-exchanged titanate nanowires as precursors. *Cryst. Growth Des.* **2010**, *10*, 2111–2115. [\[CrossRef\]](#)
43. Li, C.; Koenigsmann, C.; Ding, W.; Rudsteyn, B.; Yang, K.R.; Regan, K.P.; Konezny, S.J.; Batista, V.S.; Brudvig, G.W.; Schmuttenmaer, C.A.; et al. Facet-dependent photoelectrochemical performance of TiO₂ nanostructures: An experimental and computational study. *J. Am. Chem. Soc.* **2015**, *137*, 1520–1529. [\[CrossRef\]](#)
44. Xu, H.; Reunchan, P.; Ouyang, S.; Tong, H.; Umezawa, N.; Kako, T.; Ye, J. Anatase TiO₂ single crystals exposed with high-reactive {111} facets toward efficient H₂ evolution. *Chem. Mater.* **2013**, *25*, 405–411. [\[CrossRef\]](#)
45. Pan, J.; Liu, G.; Lu, G.Q.; Cheng, H.M. On the true photoreactivity order of {001}, {010}, and {101} facets of anatase TiO₂ crystals. *Angew. Chem. Int. Ed.* **2011**, *50*, 2133–2137. [\[CrossRef\]](#)
46. Zhang, X.; Niu, Y.; Meng, X.; Li, Y.; Zhao, J. Structural evolution and characteristics of the phase transformation between α -Fe₂O₃, Fe₃O₄ and γ -Fe₂O₃ nanoparticles under reducing and oxidizing atmospheres. *CrystEngComm* **2013**, *15*, 8166–8172. [\[CrossRef\]](#)
47. Gich, M.; Roig, A.; Taboada, E.; Molins, E.; Bonafos, C.; Snoeck, E. Stabilization of metastable phases in spatially restricted fields: The case of the Fe₂O₃ polymorphs. *Faraday Discuss.* **2007**, *136*, 345–354. [\[CrossRef\]](#)
48. Zoolfakar, A.S.; Rani, R.A.; Morfa, A.J.; O'Mullane, A.P.; Kalantar-Zadeh, K. Nanostructured copper oxide semiconductors: A perspective on materials, synthesis methods and applications. *J. Mater. Chem. C* **2014**, *2*, 5247–5270. [\[CrossRef\]](#)
49. Madelung, O. *Semiconductors: Data Handbook*, 3rd ed.; Springer: Berlin/Heidelberg, Germany; GmbH: Berlin, Germany, 2004; ISBN 9783642623325.

50. Sanson, A.; Kantor, I.; Cerantola, V.; Irifune, T.; Carnera, A.; Pascarelli, S. Local structure and spin transition in Fe₂O₃ hematite at high pressure. *Phys. Rev. B* **2016**, *94*, 2–8. [CrossRef]
51. Gupta, S.M.; Tripathi, M. A review of TiO₂ nanoparticles. *Chin. Sci. Bull.* **2011**, *56*, 1639–1657. [CrossRef]
52. Chemical Book. Available online: https://www.chemicalbook.com/ChemicalProductProperty_US_CB6115645.aspx (accessed on 30 November 2018).
53. Clark, R.J.H. *The chemistry of titanium and vanadium. An Introduction to the chemistry of the early transition elements*; Elsevier Pub. Co.: Amsterdam, The Netherlands, 1968; pp. 266–277. ISBN 978-0444406798.
54. Polyanskiy, M.N. Cu₂O Refractive Index. Available online: <https://refractiveindex.info/?shelf=main&book=Cu2O&page=Query> (accessed on 29 November 2018).
55. Polyanskiy, M.M. Fe₂O₃ refractive index. Available online: <https://refractiveindex.info/?shelf=main&book=Fe2O3&page=Query-o> (accessed on 28 November 2018).
56. Martin, G.J.; Cutting, R.S.; Vaughan, D.J.; Warren, M.C. Bulk and key surface structures of hematite, magnetite, and goethite: A density functional theory study. *Am. Miner.* **2009**, *94*, 1341–1350. [CrossRef]
57. Guo, H.; Barnard, A.S. Thermodynamic modelling of nanomorphologies of hematite and goethite. *J. Mater. Chem.* **2011**, *21*, 11566–11577. [CrossRef]
58. Mackrodt, W.C. Atomistic simulation of oxide surfaces. *Phys. Chem. Miner.* **1988**, *15*, 228–237. [CrossRef]
59. Soon, A.; Todorova, M.; Delley, B.; Stampfl, C. Thermodynamic stability and structure of copper oxide surfaces: A first-principles investigation. *Phys. Rev. B Condens. Matter Mater. Phys.* **2007**, *75*, 1–9. [CrossRef]
60. Cornell, R.M.; *The Iron Oxides: Structure, Properties, Reactions, Occurrences and Uses*; Wiley-VCH GmbH & Co KGaA: Weinheim, Germany, 2003; pp. 59–94. ISBN 9783527602094.
61. Zhu, J.; Ng, K.Y.S.; Deng, D. Micro single crystals of hematite with nearly 100% exposed {104} facets: Preferred etching and lithium storage. *Cryst. Growth Des.* **2014**, *14*, 2811–2817. [CrossRef]
62. Zheng, Z.; Huang, B.; Wang, Z.; Guo, M.; Qin, X.; Zhang, X.; Wang, P.; Dai, Y. Crystal faces of Cu₂O and their stabilities in photocatalytic reactions. *J. Phys. Chem. C* **2009**, *113*, 14448–14453. [CrossRef]
63. Chen, Z.; Lu, C. Humidity sensors: A review of materials and mechanisms. *Sens. Lett.* **2005**, *3*, 274–295. [CrossRef]
64. Lassoued, A.; Dkhil, B.; Gadri, A.; Ammar, S. Control of the shape and size of iron oxide (α-Fe₂O₃) nanoparticles synthesized through the chemical precipitation method. *Results Phys.* **2017**, *7*, 3007–3015. [CrossRef]
65. Chirita, M.; Grozescu, I. Fe₂O₃—Nanoparticles, physical properties and their photochemical and photoelectrochemical applications. *Chem. Bull. Politeh. Univ. Timisoara* **2009**, *54*, 1–8.
66. Yan, W.; Jianliang, C.; Shurong, W.; Xianzhi, G.; Jun, Z.; Huijuan, X.; Shoumin, Z.; Shihua, W. Facile synthesis of porous α-Fe₂O₃ nanorods and their application in ethanol sensors. *J. Phys. Chem. C* **2008**, *112*, 17804. [CrossRef]
67. Sun, Z.; Yuan, H.; Liu, Z.; Han, B.; Zhang, X. A highly efficient chemical sensor material for H₂S: α-Fe₂O₃ nanotubes fabricated using carbon nanotube templates. *Adv. Mater.* **2005**, *17*, 2993–2997. [CrossRef]
68. Zheng, Z.; Liao, L.; Yan, B.; Zhang, J.X.; Gong, H.; Shen, Z.X.; Yu, T. Enhanced field emission from argon plasma-treated ultra-sharp α-Fe₂O₃ nanoflakes. *Nanoscale Res. Lett.* **2009**, *4*, 1115–1119. [CrossRef]
69. Huang, J.; Yang, M.; Gu, C.; Zhai, M.; Sun, Y.; Liu, J. Hematite solid and hollow spindles: Selective synthesis and application in gas sensor and photocatalysis. *Mater. Res. Bull.* **2011**, *46*, 1211–1218. [CrossRef]
70. Goniakowski, J.; Finocchi, F.; Noguera, C. Polarity of oxide surfaces and nanostructures. *Rep. Prog. Phys.* **2008**, *71*, 1–55. [CrossRef]
71. Lu, J.; Peng, Q.; Wang, Z.; Nan, C.; Li, L.; Li, Y. Hematite nanodiscs exposing (001) facets: Synthesis, formation mechanism and application for Li-ion batteries. *J. Mater. Chem. A* **2013**, *1*, 5232–5237. [CrossRef]
72. Yi, N.; Flytzani-Stephanopoulos, M. *Catalysis by Materials with Well-Defined Structures*; Academic Press: Cambridge, MA, USA, 2015; ISBN 9780128012178.
73. Sun, S.; Zhang, X.; Yang, Q.; Liang, S.; Zhang, X.; Yang, Z. Cuprous oxide (Cu₂O) crystals with tailored architectures: A comprehensive review on synthesis, fundamental properties, functional modifications and applications. *Prog. Mater. Sci.* **2018**, *96*, 111–173. [CrossRef]
74. Wan, X.; Wang, J.; Zhu, L.; Tang, J. Gas sensing properties of Cu₂O and its particle size and morphology-dependent gas-detection sensitivity. *J. Mater. Chem. A* **2014**, *2*, 13641–13647. [CrossRef]
75. Cao, S.; Chen, H.; Han, T.; Zhao, C.; Peng, L. Rose-like Cu₂O nanoflowers via hydrothermal synthesis and their gas sensing properties. *Mater. Lett.* **2016**, *180*, 135–139. [CrossRef]

76. Zhang, L.; Cui, Z.; Wu, Q.; Guo, D.; Xu, Y.; Guo, L. Cu₂O-CuO composite microframes with well-designed micro/nano structures fabricated via controllable etching of Cu₂O microcubes for CO gas sensors. *CrystEngComm* **2013**, *15*, 7462–7467. [[CrossRef](#)]
77. Şişman, O.; Kiliç, N.; Öztürk, Z.Z. H₂ sensing properties of Cu₂O nanowires on glass substrate. *Procedia Eng.* **2015**, *120*, 1170–1174. [[CrossRef](#)]
78. Wang, L.; Zhang, R.; Zhou, T.; Lou, Z.; Deng, J.; Zhang, T. Concave Cu₂O octahedral nanoparticles as an advanced sensing material for benzene (C₆H₆) and nitrogen dioxide (NO₂) detection. *Sens. Actuators B Chem.* **2016**, *223*, 311–317. [[CrossRef](#)]
79. Cui, G.; Zhang, P.; Chen, L.; Wang, X.; Li, J.; Shi, C.; Wang, D. Highly sensitive H₂S sensors based on Cu₂O/Co₃O₄ nano/microstructure heteroarrays at and below room temperature. *Sci. Rep.* **2017**, *7*, 1–10. [[CrossRef](#)]
80. Thanh, N.T.; Maclean, N.; Mahiddine, S. Mechanisms of nucleation and growth of nanoparticles in solution. *Chem. Rev.* **2014**, *114*, 7610–7630. [[CrossRef](#)]
81. Wu, Z.; Yang, S.; Wu, W. Shape control of inorganic nanoparticles from solution. *Nanoscale* **2016**, *8*, 1237–1259. [[CrossRef](#)]
82. Mullin, J.W. *Crystallization*, 4th ed.; Butterworth-Heinemann: Oxford, MA, USA, 2001; ISBN 0 7506 4833 3.
83. Wang, F.; Richards, V.N.; Shields, S.P.; Buhro, W.E. Kinetics and mechanisms of aggregative nanocrystal growth. *Chem. Mater.* **2014**, *26*, 5–21. [[CrossRef](#)]
84. Chu, D.B.K.; Owen, J.S.; Peters, B. Nucleation and growth kinetics from LaMer burst data. *J. Phys. Chem. A* **2017**, *121*, 7511–7517. [[CrossRef](#)]
85. Huang, M.H.; Chiu, C. Achieving polyhedral nanocrystal growth with systematic shape control. *J. Mater. Chem. A* **2013**, *1*, 8081–8092. [[CrossRef](#)]
86. Geim, A.K.; Grigorieva, I.V. Van der Waals heterostructures. *Nature* **2013**, *499*, 419–425. [[CrossRef](#)]
87. Zhang, X.; Wang, K.; Wei, X.; Chen, J.-S. Carbon-Coated V₂O₅ Nanocrystals as High Performance Cathode Material for Lithium Ion Batteries. *Chem. Mater.* **2011**, *23*, 5290–5292. [[CrossRef](#)]
88. Yu, Y.; Yin, X.; Kvit, A.; Wang, X. Evolution of hollow TiO₂ nanostructures via the Kirkendall effect driven by cation exchange with enhanced photoelectrochemical performance. *Nano Lett.* **2014**, *14*, 2528–2535. [[CrossRef](#)]
89. Liu, R.; Bohannan, E.W.; Switzer, J.A.; Oba, F.; Ernst, F. Shape control in epitaxial electrodeposition: Cu₂O on InP (001). *Chem. Mater.* **2003**, *83*, 1944–1946. [[CrossRef](#)]
90. Zhu, H.; Du, M.; Yu, D.; Wang, Y.; Wang, L.; Zou, M.; Zhang, M.; Fu, Y. A new strategy for the surface-free-energy-distribution induced selective growth and controlled formation of Cu₂O-Au hierarchical heterostructures with a series of morphological evolutions. *J. Mater. Chem. A* **2013**, *1*, 919–929. [[CrossRef](#)]
91. Pang, H.; Gao, F.; Lu, Q. Morphology effect on antibacterial activity of cuprous oxide. *Chem. Commun.* **2009**, 1076–1078. [[CrossRef](#)] [[PubMed](#)]
92. Wang, S.; Yu, W.; Cheng, C.; Zhang, T.; Ge, M.; Sun, Y.; Dai, N. Fabrication of mesoporous SnO₂ nanocubes with superior ethanol gas sensing property. *Mater. Res. Bull.* **2017**, *89*, 267–272. [[CrossRef](#)]
93. Guo, W.; Sun, W.; Lv, L.P.; Kong, S.; Wang, Y. Microwave-assisted morphology evolution of Fe-based metal-organic frameworks and their derived Fe₂O₃ nanostructures for Li-ion storage. *ACS Nano* **2017**, *11*, 4198–4205. [[CrossRef](#)] [[PubMed](#)]
94. Huang, Y.; Ding, D.; Zhu, M.; Meng, W.; Huang, Y.; Geng, F.; Li, J.; Lin, J.; Tang, C.; Lei, Z.; et al. Facile synthesis of α-Fe₂O₃ nanodisk with superior photocatalytic performance and mechanism insight. *Sci. Technol. Adv. Mater.* **2015**, *16*, 14801(1)–14801(12). [[CrossRef](#)]
95. Huang, J.; Wang, L.; Gu, C.; Wang, Z.; Sun, Y.; Shim, J.J. Preparation of porous SnO₂ microcubes and their enhanced gas-sensing property. *Sens. Actuators B Chem.* **2015**, *207*, 782–790. [[CrossRef](#)]
96. Xu, H.; Wang, W.; Zhu, W. Shape evolution and size-controllable synthesis of Cu₂O octahedra and their morphology-dependent photocatalytic properties. *J. Phys. Chem. B* **2006**, *110*, 13829–13834. [[CrossRef](#)] [[PubMed](#)]
97. Liang, Y.; Shang, L.; Bian, T.; Zhou, C.; Zhang, D.; Yu, H.; Xu, H.; Shi, Z.; Zhang, T.; Wu, L.Z.; Tung, C.H. Shape-controlled synthesis of polyhedral 50-facet Cu₂O microcrystals with high-index facets. *CrystEngComm* **2012**, *14*, 4431–4436. [[CrossRef](#)]

98. Roy, N.; Park, Y.; Sohn, Y.; Leung, K.T.; Pradhan, D. Green synthesis of anatase TiO₂ nanocrystals with diverse shapes and their exposed facets-dependent photoredox activity. *ACS Appl. Mater. Interfaces* **2014**, *6*, 16498–16507. [CrossRef]
99. Wang, L.; Zang, L.; Zhao, J.; Wang, C. Green synthesis of shape-defined anatase TiO₂ nanocrystals wholly exposed with {001} and {100} facets. *Chem. Commun.* **2012**, *48*, 11736–11738. [CrossRef]
100. Li, J.; Cao, K.; Li, Q.; Xu, D. Tetragonal faceted-nanorods of anatase TiO₂ with a large percentage of active {100} facets and their hierarchical structure. *CrystEngComm* **2012**, *14*, 83–85. [CrossRef]
101. Zhou, Y.; Ding, E.Y.; Li, W.D. Synthesis of TiO₂ nanocubes induced by cellulose nanocrystal (CNC) at low temperature. *Mater. Lett.* **2007**, *61*, 5050–5052. [CrossRef]
102. Menzel, R.; Duerrbeck, A.; Liberti, E.; Yau, H.C.; McComb, D.; Shaffer, M.S.P. Determining the morphology and photocatalytic activity of two-dimensional anatase nanoplatelets using reagent stoichiometry. *Chem. Mater.* **2013**, *25*, 2137–2145. [CrossRef]
103. Yu, J.; Qi, L.; Jaroniec, M. Hydrogen production by photocatalytic water splitting over Pt/TiO₂ nanosheets with exposed 001 Facets. *J. Phys. Chem. C* **2010**, *114*, 13118–13125. [CrossRef]
104. Zhao, X.; Jin, W.; Cai, J.; Ye, J.; Li, Z.; Ma, Y.; Xie, J.; Qi, L. Shape- and size-controlled synthesis of uniform anatase TiO₂ nanocuboids enclosed by active {100} and {001} facets. *Adv. Funct. Mater.* **2011**, *21*, 3554–3563. [CrossRef]
105. Synowiec, M.; Zakrzewska, K.; Trenczek-Zajac, A.; Szczepanowicz, K.; Radecka, M.; Różycka, A.; Micek-Ilnicka, A. Functionalized structures based on shape-controlled TiO₂. *Appl. Surf. Sci.* **2018**, *473*, 603–613. [CrossRef]
106. Huang, L.; Liu, T.; Zhang, H.; Guo, W.; Zeng, W. Hydrothermal synthesis of different TiO₂ nanostructures: Structure, growth and gas sensor properties. *J. Mater. Sci. Mater. Electron.* **2012**, *23*, 2024–2029. [CrossRef]
107. Wu, N.; Wang, J.; Tafen, D.N.; Wang, H.; Zheng, J.G.; Lewis, J.P.; Liu, X.; Leonard, S.S.; Manivannan, A. Shape-enhanced photocatalytic activity of single-crystalline anatase TiO₂ (101) nanobelts. *J. Am. Chem. Soc.* **2010**, *2*, 6679–6685. [CrossRef]
108. Cozzoli, P.D.; Kornowski, A.; Weller, H. Low-temperature synthesis of soluble and processable organic-capped anatase TiO₂ nanorods. *J. Am. Chem. Soc.* **2003**, *125*, 14539–14548. [CrossRef] [PubMed]
109. Amoli, V.; Bhat, S.; Maurya, A.; Banerjee, B.; Bhaumik, A.; Sinha, A.K. Tailored synthesis of porous TiO₂ nanocubes and nano parallelepipeds with exposed 111 facets and mesoscopic void space a superior candidate for efficient dye sensitized solar cell. *ACS Appl. Mater. Interfaces* **2015**, *7*, 26022–26035. [CrossRef]
110. Gao, B.; Wan, J.; Hu, D.; Chen, Y.; Lin, B. Enhanced visible-light-driven photocatalytic performance of In₂O₃-loaded TiO₂ nanocubes with exposed (001) facet. *Chem. Res. Chin. Univ.* **2017**, *33*, 934–938. [CrossRef]
111. Ye, L.; Liu, J.; Tian, L.; Peng, T.; Zan, L. The replacement of {101} by {010} facets inhibits the photocatalytic activity of anatase TiO₂. *Appl. Catal. B Environ.* **2013**, *134–135*, 60–65. [CrossRef]
112. Zhang, Y.; Zeng, W.; Ye, H.; Li, Y. Enhanced carbon monoxide sensing properties of TiO₂ with exposed (001) facet: A combined first-principle and experimental study. *Appl. Surf. Sci.* **2018**, *442*, 507–516. [CrossRef]
113. Wu, L.; Yang, B.X.; Yang, X.H.; Chen, Z.G.; Li, Z.; Zhao, H.J.; Gong, X.Q.; Yang, H.G. On the synergistic effect of hydrohalic acids in the shape-controlled synthesis of anatase TiO₂ single crystals. *CrystEngComm* **2013**, *15*, 3252–3255. [CrossRef]
114. Wang, H.; Wu, Y.; Xu, B.Q. Preparation and characterization of nanosized anatase TiO₂ cuboids for photocatalysis. *Appl. Catal. B Environ.* **2005**, *59*, 139–146. [CrossRef]
115. Ruso, J.M.; Verdinelli, V.; Hassan, N.; Pieroni, O.; Messina, P.V. Enhancing CaP biomimetic growth on TiO₂ cuboids nanoparticles via highly reactive facets. *Langmuir* **2013**, *29*, 2350–2358. [CrossRef] [PubMed]
116. Han, X.; Wang, X.; Xie, S.; Kuang, Q.; Ouyang, J.; Xie, Z.; Zheng, L. Carbonate ions-assisted syntheses of anatase TiO₂ nanoparticles exposed with high energy (001) facets. *RSC Adv.* **2012**, *2*, 3251–3253. [CrossRef]
117. Chen, Q.; Ma, W.; Chen, C.; Ji, H.; Zhao, J. Anatase TiO₂ mesocrystals enclosed by (001) and (101) facets: Synergistic effects between Ti³⁺ and facets for their photocatalytic performance. *Chem. A Eur. J.* **2012**, *18*, 12584–12589. [CrossRef] [PubMed]
118. Dinh, C.-T.; Nguyen, T.-D.; Kleitz, F.; Do, T.-O. Shape-controlled synthesis of highly crystalline titania nanocrystals. *ASC Nano* **2009**, *3*, 3737–3743. [CrossRef]
119. Chen, C.; Hu, R.; Mai, K.; Ren, Z.; Wang, H.; Qian, G.; Wang, Z. Shape evolution of highly crystalline anatase TiO₂ nanobipyramids. *Cryst. Growth Des.* **2011**, *11*, 5221–5226. [CrossRef]

120. Wu, W.; Yang, S.; Pan, J.; Sun, L.; Zhou, J.; Dai, Z.; Xiao, X.; Zhang, H.; Jiang, C. Metal ion-mediated synthesis and shape-dependent magnetic properties of single-crystalline α -Fe₂O₃ nanoparticles. *CrystEngComm* **2014**, *16*, 5566–5572. [[CrossRef](#)]
121. Gao, F.; Liu, R.; Yin, J.; Lu, Q. Synthesis of polyhedral iron oxide nanocrystals bound by high-index facets. *Sci. China Chem.* **2014**, *57*, 114–121. [[CrossRef](#)]
122. Yang, S.; Zhou, B.; Ding, Z.; Zheng, H.; Huang, L.; Pan, J.; Wu, W.; Zhang, H. Tetragonal hematite single crystals as anode materials for high performance lithium ion batteries. *J. Power Sources* **2015**, *286*, 124–129. [[CrossRef](#)]
123. Liu, J.; Yang, S.; Wu, W.; Tian, Q.; Cui, S.; Dai, Z.; Ren, F.; Xiao, X.; Jiang, C. 3D Flowerlike α -Fe₂O₃@TiO₂ Core-Shell Nanostructures: General Synthesis and Enhanced Photocatalytic Performance. *ACS Sustain. Chem. Eng.* **2015**, *3*, 2975–2984. [[CrossRef](#)]
124. Liang, H.; Jiang, X.; Qi, Z.; Chen, W.; Wu, Z.; Xu, B.; Wang, Z.; Mi, J.; Li, Q. Hematite concave nanocubes and their superior catalytic activity for low temperature CO oxidation. *Nanoscale* **2014**, *6*, 7199–7203. [[CrossRef](#)] [[PubMed](#)]
125. Liu, R.; Jiang, Y.; Lu, Q.; Du, W.; Gao, F. Al³⁺-controlled synthesis and magnetic property of α -Fe₂O₃ nanoplates. *CrystEngComm* **2013**, *15*, 443–446. [[CrossRef](#)]
126. Kusior, A.; Michalec, K.; Jelen, P.; Radecka, M. Shaped Fe₂O₃ nanoparticles—Synthesis and enhanced photocatalytic degradation towards RhB. *Appl. Surf. Sci.* **2018**, *476*, 342–352. [[CrossRef](#)]
127. Wei, W.; Rui, H.; Fei, L.; Xintai, S.; Yanglong, H. Single-crystalline α -Fe₂O₃ nanostructures: Controlled synthesis and high-index planes-enhanced photodegradation by visible light. *J. Mater. Chem. A* **2013**, *23*, 6888–6894. [[CrossRef](#)]
128. Abdul Rashid, N.M.; Haw, C.; Chiu, W.; Khanis, N.H.; Rohaizad, A.; Khiew, P.; Abdul Rahman, S. Structural and optical-properties analysis of single crystalline hematite (α -Fe₂O₃) nanocubes prepared by one-pot hydrothermal approach. *CrystEngComm* **2016**, *18*, 4720–4732. [[CrossRef](#)]
129. Ouyang, J.; Pei, J.; Kuang, Q.; Xie, Z.; Zheng, L. Supersaturation-controlled shape evolution of α -Fe₂O₃ nanocrystals and their facet-dependent catalytic and sensing properties. *ASC Appl. Mater. Interfaces* **2014**, *6*, 12505–12514. [[CrossRef](#)] [[PubMed](#)]
130. Haiying, G.; Tifeng, J.; Qingrui, Z.; Adan, L.; Faming, G. Preparation, characterization and photocatalytic property of cubic α -Fe₂O₃ nanoparticles. *Rare Metal Mater. Eng.* **2015**, *44*, 2688–2691. [[CrossRef](#)]
131. Chen, M.; Zhao, E.; Yan, Q.; Hu, Z.; Xiao, X.; Chen, D. The effect of crystal face of Fe₂O₃ on the electrochemical performance for lithium-ion batteries. *Sci. Rep.* **2016**, *6*, 1–9. [[CrossRef](#)]
132. Liu, X.; Zhang, J.; Wu, S.; Yang, D.; Liu, P.; Zhang, H.; Wang, S.; Yao, X.; Zhu, G.; Zhao, H. Single crystal α -Fe₂O₃ with exposed {104} facets for high performance gas sensor applications. *RSC Adv.* **2012**, *2*, 6178–6184. [[CrossRef](#)]
133. Ma, J.; Lian, J.; Duan, X.; Liu, X.; Zheng, W. α -Fe₂O₃: Hydrothermal synthesis, magnetic and electrochemical properties. *J. Phys. Chem. C* **2010**, *114*, 10671–10676. [[CrossRef](#)]
134. Long, N.V.; Yang, Y.; Yuasa, M.; Thi, C.M.; Cao, Y.; Nann, T.; Nogami, M. Controlled synthesis and characterization of iron oxide nanostructures with potential applications for gas sensors and the environment. *RSC Adv.* **2014**, *4*, 6383–6390. [[CrossRef](#)]
135. Liu, Z.; Lv, B.; Wu, D.; Sun, Y.; Xu, Y. Magnetic and electrochemical behavior of rhombohedral α -Fe₂O₃ nanoparticles with {104} dominant facets. *Particuology* **2013**, *11*, 327–333. [[CrossRef](#)]
136. Liu, Z.; Lv, B.; Wu, D.; Sun, Y.; Xu, Y. Preparation and properties of octadecahedral α -Fe₂O₃ nanoparticles enclosed by {104} and {112} facets. *Eur. J. Inorg. Chem.* **2012**, 4076–4081. [[CrossRef](#)]
137. Tsai, Y.H.; Chanda, K.; Chu, Y.T.; Chiu, C.Y.; Huang, M.H. Direct formation of small Cu₂O nanocubes, octahedra, and octapods for efficient synthesis of triazoles. *Nanoscale* **2014**, *6*, 8704–8709. [[CrossRef](#)]
138. Li, P.; Ji, J.; Deng, X.; Li, A.; Hu, J.; Li, G.; Zhang, W. Fe₂O₃ icositetrahedra: Evolution and their comparative photocatalytic activities. *CrystEngComm* **2015**, *17*, 7283–7289. [[CrossRef](#)]
139. Tang, L.; Lv, J.; Kong, C.; Yang, Z.; Li, J. Facet-dependent nonenzymatic glucose sensing properties of Cu₂O cubes and octahedra. *New J. Chem.* **2016**, *40*, 6573–6576. [[CrossRef](#)]
140. Pande, S.; Jana, S.; Basu, S.; Sinha, A.K.; Datta, A.; Pal, T. Nanoparticle-catalyzed clock reaction. *J. Phys. Chem. C* **2008**, *112*, 3619–3626. [[CrossRef](#)]

141. Sui, Y.; Fu, W.; Yang, H.; Zeng, Y.; Zhang, Y.; Zhao, Q.; Li, Y.; Zhou, X.; Leng, Y.; Li, M.; et al. Low temperature synthesis of Cu₂O crystals: Shape evolution and growth mechanism. *Cryst. Growth Des.* **2010**, *10*, 99–108. [\[CrossRef\]](#)
142. Shang, Y.; Sun, D.; Shao, Y.; Zhang, D.; Guo, L.; Yang, S. A facile top-down etching to create a Cu₂O jagged polyhedron covered with numerous {110} edges and {111} corners with enhanced photocatalytic activity. *Chem. A Eur. J.* **2012**, *18*, 14261–14266. [\[CrossRef\]](#)
143. Tsai, Y.H.; Chiu, C.Y.; Huang, M.H. Fabrication of diverse Cu₂O nanoframes through face-selective etching. *J. Phys. Chem. C* **2013**, *117*, 24611–24617. [\[CrossRef\]](#)
144. Zhong, Y.; Li, Y.; Li, S.; Feng, S.; Zhang, Y. Nonenzymatic hydrogen peroxide biosensor based on four different morphologies of cuprous oxide nanocrystals. *RSC Adv.* **2014**, *4*, 40638–40642. [\[CrossRef\]](#)
145. Kuo, C.; Huang, M.H. Fabrication of truncated rhombic dodecahedral Cu₂O nanocages and nanoframes by particle aggregation and acidic etching. *J. Am. Chem. Soc.* **2008**, 12815–12820. [\[CrossRef\]](#)
146. Chanda, K.; Rej, S.; Huang, M.H. Facet-dependent catalytic activity of Cu₂O nanocrystals in the one-pot synthesis of 1,2,3-triazoles by multicomponent click reactions. *Chem. A Eur. J.* **2013**, *19*, 16036–16043. [\[CrossRef\]](#)
147. Bujan, M.; Sikirić, M.; Filipović-Vinceković, N.; Vdović, N.; Garti, N.; Füredi-Milhofer, H. Effect of anionic surfactants on crystal growth of calcium hydrogen phosphate dihydrate. *Langmuir* **2001**, *17*, 6461–6470. [\[CrossRef\]](#)
148. Liu, X.; Sui, Y.; Yang, X.; Jiang, L.; Wang, F.; Wei, Y.; Zou, B. A feasible approach to synthesize Cu₂O microcrystals and their enhanced non-enzymatic sensor performance. *RSC Adv.* **2015**, *5*, 59099–59105. [\[CrossRef\]](#)
149. Han, X.; Liao, F.; Zhang, Y.; Yuan, Z.; Chen, H.; Xu, C. Rapid and template-free synthesis of Cu₂O truncated octahedra using glucose as green reducing agent. *Mater. Lett.* **2018**, *210*, 31–34. [\[CrossRef\]](#)
150. Kim, M.C.; Kim, S.J.; Han, S.B.; Kwak, D.H.; Hwang, E.T.; Kim, D.M.; Lee, G.H.; Choe, H.S.; Park, K.W. Cubic and octahedral Cu₂O nanostructures as anodes for lithium-ion batteries. *J. Mater. Chem. A* **2015**, *3*, 23003–23010. [\[CrossRef\]](#)
151. Gao, H.; Zhang, J.; Li, M.; Liu, K.; Guo, D.; Zhang, Y. Evaluating the electric property of different crystal faces and enhancing the Raman scattering of Cu₂O microcrystal by depositing Ag on the surface. *Curr. Appl. Phys.* **2013**, *13*, 935–939. [\[CrossRef\]](#)
152. Sun, S.; Kong, C.; You, H.; Song, X.; Ding, B.; Yang, Z. Facet-selective growth of Cu-Cu₂O heterogeneous architectures. *CrystEngComm* **2012**, *14*, 40–43. [\[CrossRef\]](#)
153. Tian, F.; Zhang, Y.; Zhang, J.; Pan, C. Raman spectroscopy: A new approach to measure the percentage of anatase TiO₂ exposed (001) facets. *J. Phys. Chem. C* **2012**, *116*, 7515–7519. [\[CrossRef\]](#)
154. Sun, S.; Kong, C.; Yang, S.; Wang, L.; Song, X.; Ding, B.; Yang, Z. Highly symmetric polyhedral Cu₂O crystals with controllable-index planes. *CrystEngComm* **2011**, *13*, 2217–2221. [\[CrossRef\]](#)
155. Zhang, Y.; Deng, B.; Zhang, T.; Gao, D.; Xu, A.W. The crystal-facet-dependent effect of polyhedral Cu₂O microcrystals on photocatalytic activity. *J. Phys. Chem. C* **2010**, *114*, 5073–5079. [\[CrossRef\]](#)
156. Zhang, D.F.; Zhang, H.; Guo, L.; Zheng, K.; Han, X.D.; Zhang, Z. Delicate control of crystallographic facet-oriented Cu₂O nanocrystals and the correlated adsorption ability. *J. Mater. Chem.* **2009**, *19*, 5220–5225. [\[CrossRef\]](#)
157. Jie, Z.; Nosaka, Y. Mechanism of the OH radical generation in photocatalysis with TiO₂ of different crystalline Types. *J. Phys. Chem. C* **2014**, *20*, 10824–10832. [\[CrossRef\]](#)
158. Nosaka, Y.; Nosaka, A. Understanding hydroxyl radical (•OH) generation processes in photocatalysis. *ACS Energy Lett.* **2016**, *1*, 356–359. [\[CrossRef\]](#)
159. Tachikawa, T.; Majima, T. Metal oxide mesocrystals with tailored structures and properties for energy conversion and storage applications. *NPG Asia Mater.* **2014**, *6*, 1–11. [\[CrossRef\]](#)
160. Batzill, M.; Katsiev, K.; Burst, J.M.; Diebold, U.; Chaka, A.M.; Delley, B. Gas-phase-dependent properties of SnO₂ (110), (100), and (101) single-crystal surfaces: Structure, composition, and electronic properties. *Phys. Rev. B Condens. Matter Mater. Phys.* **2005**, *72*, 1–20. [\[CrossRef\]](#)
161. Li, J.; Wu, N. Semiconductor-based photocatalysts and photoelectrochemical cells for solar fuel generation: A review. *Catal. Sci. Technol.* **2015**, *5*, 1360–1384. [\[CrossRef\]](#)
162. Xie, Y.P.; Liu, G.; Yin, L.; Cheng, H.M. Crystal facet-dependent photocatalytic oxidation and reduction reactivity of monoclinic WO₃ for solar energy conversion. *J. Mater. Chem.* **2012**, *22*, 6746–6751. [\[CrossRef\]](#)

163. Jiang, W.; Pang, Y.; Gu, L.; Yao, Y.; Su, Q.; Ji, W.; Au, C.T. Structurally defined SnO₂ substrates, nanostructured Au/SnO₂ interfaces, and their distinctive behavior in benzene and methanol oxidation. *J. Catal.* **2017**, *349*, 183–196. [\[CrossRef\]](#)
164. Shi, J.; Hu, G.; Cong, R.; Bu, H.; Dai, N. Controllable synthesis of WO₃·nH₂O microcrystals with various morphologies by a facile inorganic route and their photocatalytic activities. *New J. Chem.* **2013**, *37*, 1538–1544. [\[CrossRef\]](#)
165. Huang, Q.; Zhang, S.; Cai, C.; Zhou, B. β- and α-Bi₂O₃ nanoparticles synthesized via microwave-assisted method and their photocatalytic activity towards the degradation of rhodamine B. *Mater. Lett.* **2011**, *65*, 988–990. [\[CrossRef\]](#)
166. Wu, Y.C.; Chaing, Y.C.; Huang, C.Y.; Wang, S.F.; Yang, H.Y. Morphology-controllable Bi₂O₃ crystals through an aqueous precipitation method and their photocatalytic performance. *Dye. Pigment.* **2013**, *98*, 25–30. [\[CrossRef\]](#)
167. Li, R.; Han, H.; Zhang, F.; Wang, D.; Li, C. Highly efficient photocatalysts constructed by rational assembly of dual-cocatalysts separately on different facets of BiVO₄. *Energy Environ. Sci.* **2014**, *7*, 1369–1376. [\[CrossRef\]](#)
168. Zhao, Y.; Li, R.; Mu, L.; Li, C. Significance of crystal morphology controlling in semiconductor-based photocatalysis: A case study on BiVO₄ Photocatalyst. *Cryst. Growth Des.* **2017**, *17*, 2923–2928. [\[CrossRef\]](#)
169. Zheng, Z.; Huang, B.; Lu, J.; Qin, X.; Zhang, X.; Dai, Y. Hierarchical TiO₂ microspheres: Synergetic effect of {001} and {101} facets for enhanced photocatalytic activity. *Chem. A Eur. J.* **2011**, *17*, 15032–15038. [\[CrossRef\]](#)
170. Xiang, Q.; Lv, K.; Yu, J. Pivotal role of fluorine in enhanced photocatalytic activity of anatase TiO₂ nanosheets with dominant (001) facets for the photocatalytic degradation of acetone in air. *Appl. Catal. B Environ.* **2010**, *96*, 557–564. [\[CrossRef\]](#)
171. Tachikawa, T.; Wang, N.; Yamashita, S.; Cui, S.C.; Majima, T. Design of a highly sensitive fluorescent probe for interfacial electron transfer on a TiO₂ surface. *Angew. Chem. Int. Ed.* **2010**, *49*, 8593–8597. [\[CrossRef\]](#)
172. Avgouropoulos, G.; Ioannides, T.; Papadopolou, C.; Batista, J.; Hocevar, S.; Matralis, H.K. A comparative study of the C₃H₆+NO+O₂, C₃H₆+O₂ and NO+O₂ reactions in excess oxygen over Na-modified Pt/g-Al₂O₃ catalysts. *Catal. Today* **2002**, *75*, 157–167. [\[CrossRef\]](#)
173. Kiely, C.J.; Hodge, N.A.; Hutchings, G.J.; Golunski, S.E.; Whyman, R.; Pankhurst, Q.A.; Wagner, F.E.; Rajaram, R.R. Microstructural comparison of calcined and uncalcined gold/iron-oxide catalysts for low-temperature CO oxidation. *Catal. Today* **2002**, *72*, 133–144. [\[CrossRef\]](#)
174. Grenfell, J.L.; Stock, J.W.; Patzer, A.B.C.; Gebauer, S.; Rauer, H. Oxidation of CO on surface hematite in high CO₂ atmospheres. *Earth Planet. Astrophys.* **2010**, 1–26. [\[CrossRef\]](#)
175. Sun, L.; Zhan, W.; Li, Y.-A.; Wang, F.; Zhang, X.; Han, X. Understanding the facet-dependent catalytic performance of hematite microcrystals in a CO oxidation reaction. *Inorg. Chem. Front.* **2018**, *5*, 2332–2339. [\[CrossRef\]](#)
176. Chan, J.Y.T.; Ang, S.Y.; Ye, E.Y.; Sullivan, M.; Zhang, J.; Lin, M. Heterogeneous photo-Fenton reaction on hematite (α-Fe₂O₃) {104}, {113} and {001} surface facets. *Phys. Chem. Chem. Phys.* **2015**, *17*, 25333–25341. [\[CrossRef\]](#)
177. Rehman, S.; Yang, W.; Liu, F.; Hong, Y.; Wang, T.; Hou, Y. Facile synthesis of anisotropic single crystalline α-Fe₂O₃ nanoplates and their facet-dependent catalytic performance. *Inorg. Chem. Front.* **2015**, *2*, 576–583. [\[CrossRef\]](#)
178. Xie, S.; Jia, H.; Lu, F.; Sun, N.; Yu, J.; Liu, S.; Zheng, L. Controlled synthesis of α-Fe₂O₃ nanostructures with the assistance of ionic liquid and their distinct photocatalytic performance under visible-light irradiation. *CrystEngComm* **2015**, *17*, 1210–1218. [\[CrossRef\]](#)
179. Kuo, C.-H.; Huang, M.H. Facile synthesis of Cu₂O nanocrystals with systematic shape evolution from cubic to octahedral structures. *J. Phys. Chem. C* **2008**, *112*, 31. [\[CrossRef\]](#)
180. Huang, W.-C.; Lyu, L.-M.; Yang, Y.-C.; Huang, M.H. Synthesis of Cu₂O nanocrystals from cubic to rhombic dodecahedral structures and their comparative photocatalytic activity. *J. Am. Chem. Soc.* **2012**, *134*, 1261–1267. [\[CrossRef\]](#)
181. Ho, J.Y.; Huang, M.H. Synthesis of submicrometer-sized Cu₂O crystals with morphological evolution from cubic to hexapod structures and their comparative photocatalytic activity. *J. Phys. Chem. C* **2009**, *113*, 14159–14164. [\[CrossRef\]](#)
182. Sun, S.; Song, X.; Sun, Y.; Deng, D.; Yang, Z. The crystal-facet-dependent effect of polyhedral Cu₂O microcrystals on photocatalytic activity. *Catal. Sci. Technol.* **2012**, *2*, 925–930. [\[CrossRef\]](#)

183. Xu, Y.; Wang, H.; Yu, Y.; Tian, L.; Zhao, W.; Zhang, B. Cu₂O nanocrystals: surfactant-free room-temperature morphology-modulated synthesis and shape-dependent heterogeneous organic catalytic activities. *J. Phys. Chem. C* **2011**, *115*, 15288–15296. [\[CrossRef\]](#)
184. Leng, M.; Yu, C.; Wang, C. Polyhedral Cu₂O particles: Shape evolution and catalytic activity on cross-coupling reaction of iodobenzene and phenol. *CrystEngComm* **2012**, *14*, 8454–8461. [\[CrossRef\]](#)
185. Li, L.; Nan, C.; Peng, Q.; Li, Y. Selective synthesis of Cu₂O nanocrystals as shape-dependent catalysts for oxidative arylation of phenylacetylene. *Chem. A Eur. J.* **2012**, *18*, 10491–10496. [\[CrossRef\]](#)
186. Pang, H.; Gao, F.; Lu, Q. Glycine-assisted double-solvothermal approach for various cuprous oxide structures with good catalytic activities. *CrystEngComm* **2010**, *12*, 406–412. [\[CrossRef\]](#)
187. Leng, M.; Liu, M.; Zhang, Y.; Wang, Z.; Yu, C.; Yang, X.; Zhang, H.; Wang, C. Polyhedral 50-facet Cu₂O microcrystals partially enclosed by {311} high-index planes: Synthesis and enhanced catalytic CO oxidation activity. *J. Am. Chem. Soc.* **2010**, *132*, 17084–17087. [\[CrossRef\]](#) [\[PubMed\]](#)
188. Meldal, M.P.; Meldal, M.; Tornøe, C.W. Cu-catalyzed azide—Alkyne cycloaddition Cu-catalyzed azide—alkyne cycloaddition. *Chem. Rev.* **2017**, *108*, 2952–3015. [\[CrossRef\]](#)
189. Kolb, H.C.; Sharpless, K.B. The growing impact of click chemistry on drug discovery. *Drug Deliv. Today* **2003**, *8*, 1128–1137. [\[CrossRef\]](#)
190. Park, H.; Kim, H.I.; Moon, G.H.; Choi, W. Photoinduced charge transfer processes in solar photocatalysis based on modified TiO₂. *Energy Environ. Sci.* **2016**, *9*, 411–433. [\[CrossRef\]](#)
191. Wang, L.; Ge, J.; Wang, A.; Deng, M.; Wang, X.; Bai, S.; Li, R.; Jiang, J.; Zhang, Q.; Luo, Y.; Xiong, Y. Designing p-type semiconductor-metal hybrid structures for improved photocatalysis. *Angew. Chem. Int. Ed.* **2014**, *53*, 5107–5111. [\[CrossRef\]](#)
192. Gaskov, A.M.; Rumyantseva, M.N. Nature of gas sensitivity in nanocrystalline metal oxides. *Russ. J. Appl. Chem.* **2001**, *74*, 440–444. [\[CrossRef\]](#)
193. Yamazoe, N.; Shimanoe, K. Theoretical approach to the rate of response of semiconductor gas sensor. *Sens. Actuators B Chem.* **2010**, *150*, 132–140. [\[CrossRef\]](#)
194. Zhao, Q.; Shen, Q.; Yang, F.; Zhao, H.; Liu, B.; Liang, Q.; Wei, A.; Yang, H.; Liu, S. Direct growth of ZnO nanodisk networks with an exposed (0001) facet on Au comb-shaped interdigitating electrodes and the enhanced gas-sensing property of polar {0001} surfaces. *Sens. Actuators B Chem.* **2014**, *195*, 71–79. [\[CrossRef\]](#)
195. Yang, Y.; Liang, Y.; Wang, G.; Liu, L.; Yuan, C.; Yu, T.; Li, Q.; Zeng, F.; Gu, G. Enhanced gas-sensing properties of the hierarchical TiO₂ hollow microspheres with exposed high-energy {001} crystal facets. *ACS Appl. Mater. Interfaces* **2015**, *7*, 24902–24908. [\[CrossRef\]](#)
196. Yang, Y.; Hong, A.; Liang, Y.; Xu, K.; Yu, T.; Shi, J.; Zeng, F.; Qu, Y.; Liu, Y.; Ding, M.; Zhang, W.; Yuan, C. High-energy {001} crystal facets and surface fluorination engineered gas sensing properties of anatase titania nanocrystals. *Appl. Surf. Sci.* **2017**, *423*, 602–610. [\[CrossRef\]](#)
197. Das, S.; Jayaraman, V. SnO₂: A comprehensive review on structures and gas sensors. *Prog. Mater. Sci.* **2014**, *66*, 112–255. [\[CrossRef\]](#)
198. Gurlo, A. Nanosensors: Towards morphological control of gas sensing activity. SnO₂, In₂O₃, ZnO and WO₃ case studies. *Nanoscale* **2011**, *3*, 154–165. [\[CrossRef\]](#)
199. Wang, C.; Cai, D.; Liu, B.; Li, H.; Wang, D.; Liu, Y.; Wang, L.; Wang, Y.; Li, Q.; Wang, T. Ethanol-sensing performance of tin dioxide octahedral nanocrystals with exposed high-energy {111} and {332} facets. *J. Mater. Chem. A* **2014**, *2*, 10623–10628. [\[CrossRef\]](#)
200. Han, X.; Zheng, L.; Jin, M.; Jiang, Y.; Kuang, Q.; Xie, Z.; Jiang, Z.; Xie, S. Synthesis of tin dioxide octahedral nanoparticles with exposed high-energy {221} facets and enhanced gas-sensing properties. *Angew. Chem. Int. Ed.* **2009**, *48*, 9180–9183. [\[CrossRef\]](#)
201. Xu, J.; Xiang, Q.; Xue, Z.; Qin, N.; Cheng, Z. The crystal facet-dependent gas sensing properties of ZnO nanosheets: Experimental and computational study. *Sensors Actuators B Chem.* **2016**, *242*, 148–157. [\[CrossRef\]](#)
202. Li, W.; Xu, H.; Yu, H.; Zhai, T.; Xu, Q.; Yang, X.; Wang, J.; Cao, B. Different morphologies of ZnO and their triethylamine sensing properties. *J. Alloys Compd.* **2017**, *706*, 461–469. [\[CrossRef\]](#)
203. Qin, N.; Xiang, Q.; Zhao, H.; Zhang, J.; Xu, J. Evolution of ZnO microstructures from hexagonal disk to prismoid, prism and pyramid and their crystal facet-dependent gas sensing properties. *CrystEngComm* **2014**, *16*, 7062–7073. [\[CrossRef\]](#)

204. Kaneti, Y.V.; Zhang, Z.; Yue, J.; Zakaria, Q.M.D.; Chen, C.; Jiang, X.; Yu, A. Crystal plane-dependent gas-sensing properties of zinc oxide nanostructures: Experimental and theoretical studies. *Phys. Chem. Chem. Phys.* **2014**, *16*, 11471–11480. [CrossRef]
205. Han, X.G.; He, H.Z.; Kuang, Q.; Zhou, X.; Zhang, X.H.; Xu, T.; Xie, Z.X.; Zheng, L.S. Controlling morphologies and tuning the related properties of nano/microstructured ZnO crystallites. *J. Phys. Chem. C* **2009**, *113*, 584–589. [CrossRef]
206. Patil, V.L.; Bhosale, J.L.; Shendage, S.S.; Vanalakar, S.A.; Patil, S.P.; Patil, P.S.; Kim, J.H.; Harale, N.S. Sensitive and selective NO₂ gas sensor based on WO₃ nanoplates. *Sens. Actuators B Chem.* **2016**, *240*, 426–433. [CrossRef]
207. Gong, J.; Li, Y.; Hu, Z.; Zhou, Z.; Deng, Y. Ultrasensitive NH₃ gas sensor from polyaniline nanograin enched TiO₂ fibers. *J. Phys. Chem. C* **2010**, *114*, 9970–9974. [CrossRef]
208. Devi, G.S.; Hyodo, T.; Shimizu, Y.; Egashira, M. Synthesis of mesoporous TiO₂-based powders and their gas-sensing properties. *Sens. Actuators B Chem.* **2002**, *87*, 122–129. [CrossRef]
209. Carney, C.M.; Yoo, S.; Akbar, S.A. TiO₂-SnO₂ nanostructures and their H₂ sensing behavior. *Sens. Actuators B Chem.* **2005**, *108*, 29–33. [CrossRef]
210. Della Gaspera, E.; Guglielmi, M.; Agnoli, S.; Granozzi, G.; Post, M.L.; Bello, V.; Mattei, G.; Martucci, A. Au nanoparticles in nanocrystalline TiO₂-NiO films for SPR-based, selective H₂S gas sensing. *Chem. Mater.* **2010**, *22*, 3407–3417. [CrossRef]
211. Barreca, D.; Carraro, G.; Comini, E.; Gasparotto, A.; MacCato, C.; Sada, C.; Sberveglieri, G.; Tondello, E. Novel synthesis and gas sensing performances of CuO-TiO₂ nanocomposites functionalized with Au nanoparticles. *J. Phys. Chem. C* **2011**, *115*, 10510–10517. [CrossRef]
212. Tang, H.; Prasad, K.; Sanjines, R.; Levy, F. TiO₂ anatase thin films as gas sensors. *Sens. Actuators B Chem.* **1995**, *26–27*, 71–75. [CrossRef]
213. Sclafani, A.; Herrmann, J.M. Comparison of the photoelectronic and photocatalytic activities of various anatase and rutile forms of titania in pure liquid organic phases and in aqueous solutions. *J. Phys. Chem.* **1996**, *100*, 13655–13661. [CrossRef]
214. Yang, G.; Hu, P.; Cao, Y.; Yuan, F.; Xu, R. Fabrication of porous TiO₂ hollow spheres and their application in gas sensing. *Nanoscale Res. Lett.* **2010**, *5*, 1437–1441. [CrossRef]
215. Galstyan, V.; Comini, E.; Faglia, G.; Sberveglieri, G. TiO₂ nanotubes: Recent advances in synthesis and gas sensing properties. *Sensors* **2013**, *13*, 14813–14838. [CrossRef]
216. Zakrzewska, K.; Radecka, M. TiO₂-Based Nanomaterials for Gas Sensing—Influence of Anatase and Rutile Contributions. *Nanoscale Res. Lett.* **2017**, *12*, 89–96. [CrossRef]
217. Cukierman, S. Et tu, Grotthuss! and other unfinished stories. *Biochim. Biophys. Acta Bioenerg.* **2006**, *1757*, 876–885. [CrossRef]
218. Španěl, P.; Smith, D. Reactions of hydrated hydronium ions and hydrated hydroxide ions with some hydrocarbons and oxygen-bearing organic molecules. *J. Phys. Chem.* **1995**, *99*, 15551–15556. [CrossRef]
219. Chaplin, M. Water structure and science. Available online: <http://www1.lsbu.ac.uk/water/grotthuss.html> (accessed on 19 March 2019).
220. Cuong, N.D.; Khieu, D.Q.; Hoa, T.T.; Quang, D.T.; Viet, P.H.; Lam, T.D.; Hoa, N.D.; Hieu, N.V. Facile synthesis of α-Fe₂O₃ nanoparticles for high-performance CO gas sensor. *Mater. Res. Bull.* **2015**, *68*, 302–307. [CrossRef]
221. Wu, Z.; Yu, K.; Zhangand, S.; Xie, Y. Hematite hollow spheres with a mesoporous shell: Controlled synthesis and applications in gas sensor and lithium ion batteries. *J. Phys. Chem. C* **2008**, *112*, 11307–11313. [CrossRef]
222. Yan, H.; Su, X.; Yang, C.; Wang, J.; Niu, C. Improved photocatalytic and gas sensing properties of α-Fe₂O₃ nanoparticles derived from β-FeOOH nanospindles. *Ceram. Int.* **2014**, *40*, 1729–1733. [CrossRef]
223. Barsan, N.; Simion, C.; Heine, T.; Pokhrel, S.; Weimar, U. Modeling of sensing and transduction for p-type semiconducting metal oxide based gas sensors. *J. Electroceram.* **2010**, *25*, 11–19. [CrossRef]
224. Hübner, M.; Simion, C.E.; Tomescu-Stănoiu, A.; Pokhrel, S.; Bărsan, N.; Weimar, U. Influence of humidity on CO sensing with p-type CuO thick film gas sensors. *Sens. Actuators B Chem.* **2011**, *153*, 347–353. [CrossRef]
225. Mazhar, M.E.; Faglia, G.; Comini, E.; Zappa, D.; Baratto, C.; Sberveglieri, G. Kelvin probe as an effective tool to develop sensitive p-type CuO gas sensors. *Sens. Actuators B Chem.* **2016**, *222*, 1257–1263. [CrossRef]
226. Meng, F.N.; Di, X.P.; Dong, H.W.; Zhang, Y.; Zhu, C.L.; Li, C.; Chen, Y.J. Ppb H₂S gas sensing characteristics of Cu₂O/CuO sub-microspheres at low-temperature. *Sens. Actuators B Chem.* **2013**, *182*, 197–204. [CrossRef]

- 227. Zhang, J.; Liu, J.; Peng, Q.; Wang, X.; Li, Y. Nearly monodisperse Cu₂O and CuO nanospheres: Preparation and applications for sensitive gas sensors. *Chem. Mater.* **2006**, *18*, 867–871. [[CrossRef](#)]
- 228. Shishiyanu, S.T.; Shishiyanu, T.S.; Lupan, O.I. Novel NO₂ gas sensor based on cuprous oxide thin films. *Sens. Actuators B Chem.* **2006**, *113*, 468–476. [[CrossRef](#)]
- 229. Liu, J.; Wang, S.; Wang, Q.; Geng, B. Microwave chemical route to self-assembled quasi-spherical Cu₂O microarchitectures and their gas-sensing properties. *Sens. Actuators B Chem.* **2009**, *143*, 253–260. [[CrossRef](#)]
- 230. Lin, Y.; Cui, X.; Li, L. Low-potential amperometric determination of hydrogen peroxide with a carbon paste electrode modified with nanostructured cryptomelane-type manganese oxides. *Electrochem. Commun.* **2005**, *7*, 166–172. [[CrossRef](#)]
- 231. Bahnemann, D.W.; Hoffmann, M.R.; Hong, A.P.; Kormann, C. *Photocatalytic formation of hydrogen peroxide. In The Chemistry of Acid Rain*; American Chemical Society: Washington, DC, USA, 1987; pp. 120–132. [[CrossRef](#)]



© 2019 by the authors. Licensee MDPI, Basel, Switzerland. This article is an open access article distributed under the terms and conditions of the Creative Commons Attribution (CC BY) license (<http://creativecommons.org/licenses/by/4.0/>).